Journal of Ship Research, Vol. 57, No. 4, December 2013
http://dx.doi.org/10.5957/JOSR.57.4.110040

Unified Rotor Lifting Line Theory

Brenden P. Epps[†](✉) and **Richard W. Kimball**[‡]

[†] *Thayer School of Engineering, Dartmouth College, Hanover, New Hampshire, USA*
[‡] *Department of Engineering, Maine Maritime Academy, Castine, Maine, USA*

Abstract

A unified lifting line method for the design and analysis of axial flow propellers and turbines is presented. The method incorporates significant improvements to the classical lifting line methods for propeller design to extend the method to the design of turbines. In addition, lifting line analysis methods are developed to extend the usefulness of the lifting line model to allow generation of performance curves for off-design analysis. The result is a fast computational methodology for the design and analysis of propellers or turbines that can be used in preliminary design and parametric studies. Design and analysis validation cases are presented and compared to experimental data.

1 Introduction

This manuscript presents a unified rotor lifting line model based on numerical vortex lattice theory that can be used for the optimization and analysis of both propellers and turbines. The major contributions of this work can be summarized as follows:

- Improved lifting line design method for axial flow propellers,
- Implementation of lifting line design for axial flow turbines,
- Development of a lifting line analysis capability for propellers and turbines,
- Validation of these methods against experiment and prior methods.

Lifting line methods, due to their computational efficiency, have for many years been a key part of the design process for propellers as preliminary parametric design tools. The output of the typical lifting line design provides a starting design for more sophisticated lifting surface blade design, panel method analysis, and computational fluid dynamics (CFD) analysis. The lifting line method produces accurate prediction of rotor forces and efficiency and quickly converges to optimal rotor parameters such as diameter, rotation rate and blade number. This makes the lifting line approach suitable for parametric studies and system level design. The main limitation of lifting line design method is in the accuracy of the output blade geometry, so lifting-surface geometry corrections are incorporated herein to account for finite-aspect-ratio effects.

While axial-flow turbines are fundamentally no different than propellers, lifting line theory is typically not used in turbine design (in favor of blade element momentum theory). However, lifting line theory offers several advantages over turbine blade element momentum theory (BEM), such as a more accurate relationship between the induction velocities and the radial circulation distribution. This makes the lifting line model particularly attractive for problems such as cavitation analysis of marine hydrokinetic turbines. Also, like the BEM, the lifting line model is directly extendable to the coupled aerodynamic, structural, and controls analysis of large wind turbines, and thus, it forms a strong foundation on which to build more advanced multi-physics analysis tools. Thus, a second thrust of this work applies the lifting line model to the axial flow turbine case. In doing so, this work presents a unified rotor lifting line model, which is capable of handling both the propeller and turbine applications.

The standard rotor design problem involves determining the radial circulation distribution that either (a) minimizes propeller torque for a specified thrust, or (b) maximizes turbine torque. From a philosophical standpoint, these problems are nearly identical, so one could ask: can a single design methodology be developed that can be used for the optimization of both propellers and turbines? Indeed, the answer is yes, and the hybrid design algorithm is developed and discussed herein, within the context of more traditional propeller and turbine design algorithms.

In addition to making improvements in the design problem, for which lifting line methods have existed for some time (Lerbs, 1952; Coney, 1989, e.g.), the present work also extends the lifting line approach to the performance analysis of propellers and turbines over their entire range of operation.

In the design and analysis of rotors, there are three overarching problems of interest:

(inputs)→(design)
(design)→(geometry)
(geometry)→(states)

The typical "inputs" to a rotor design are parameters such as inflow velocity distribution, rotation speed, diameter, required thrust (of a propeller), etc. The "design" consists of distributions of circulation, chord, lift coefficient, etc. versus radius: Kerwin, Coney, and Hsin (1986) addressed the problem of (inputs)→(design) for the propeller case, optimizing the circulation distribution to maximize efficiency. Others have addressed "design" optimization for the turbine case (Falcão de Campos, 2007; Xu and Kinnas, 2010, e.g.), and new methods for this purpose are developed herein. Coney (1989) has addressed the problem of (design)→(geometry), and his methods have been adopted herein. The design point is one of many possible "states", where a "state" is a physically-consistent set of wind speed, rotation speed, circulation distribution, etc. (that does not necessarily correspond to the design point). Each point on the performance curve represents one "state" of the system. Many methods exist to solve the problem of (geometry)→(states), one such lifting-line method being that of (Kerwin, 1959). However, as Epps (2010a) shows, one can skip the intermediate "geometry" step and find the off-design performance curve directly from the design-point performance:

(design)→(states)

The present method extends the work of (Epps, 2010a), now including the capability of (geometry)→(states) analysis, as well as employing more accurate corrections for finite-aspect-ratio effects.

The performance analysis approach presented herein uses the power of the lifting line method in computing the rotor flowfield, including induced velocities which are critical for the analysis of blade forces. Then 2D foil lift and drag models, corrected for the 3D inflow are used to compute the blade forces and ultimately the rotor forces and efficiency. Analysis capability allows for the generation of typical performance curves for propellers (i.e K_T vs. J_s) and turbines (C_P vs. λ)). This allows the method to be used for off design analysis and allows the method to be incorporated into system-level engineering tools such as integrated ship design codes.

Interestingly, the wind turbine community typically does not follow the (inputs) → (design) → (geometry) → (states) workflow. Turbine geometry optimization is typically performed via genetic algorithm (i.e. computing the states and then overall performance for randomly-generated geometries), which is essentially (inputs) → (geometry) → (states) (Sale, 2010; Buhl, 2011). While the flexibility of the genetic algorithm affords flexibility with regards to the multi-objective nature of the turbine design optimization problem, it does not provide a rigorous analytical framework to verify that the converged design is in fact the optimum solution. Thus, a second thrust of the present work is to apply the concepts of propeller lifting line theory to the turbine design problem, providing an analytic framework by which to address the turbine design problem:

(inputs)→(design)

For both design and analysis modes, the present method provides detailed rotor information such as velocity fields or blade pressure distributions. Such information can be useful for cavitation analysis, blade stress analysis, or wake field studies for turbine array design. Examples of cavitation analysis using the methodology can be found in (Epps et al, 2011) and the implementation of stress analysis can be found in (Ketcham, 2010).

The blade section algorithms used in analysis are modular and can be adopted from sources such as blade section libraries or generated through coupling with blade section solvers such as XFOIL (Drela, 1989). In addition, lifting line camber corrections developed by Morgan et al (1968) have been included in the geometry generation and analysis modules to allow the analysis of existing rotor geometries with reasonable accuracy. Examples of geometry analysis are presented.

The method has also been extended to the design and analysis of multi-component rotors. For example, an implementation of the methods for the design of contra-rotating propellers (CRP) can be found in (Laskos, 2010), and the CRP performance analysis was implemented by Kravitz (2011). Efforts to incorporate ducted rotors have also been implemented by Stubblefield (2008), and experimental validation of ducted rotors is also a current effort.

The present methods have been implemented in the open-source numerical code `OpenProp v3.0` (Epps and Kimball, 2013), which is used for all calculations herein.

This article is organized as follows. In §2, the unified rotor lifting line model is presented. In §3, the optimization of both propellers and turbines is considered, and a hybrid lifting-line/blade-element-momentum rotor optimization method is presented in §3.5. Examples illustrating the design of optimized rotors are presented in §4. In §5, the performance

analysis method is described. Finally, §6 presents examples illustrating the off-design performance of propellers and turbines.

2 Rotor lifting-line model

This section presents a unified rotor lifting-line model that can be used for both propeller and turbine design and analysis. The sign conventions are developed with respect to the propeller, and it is noted what signs must change to represent the turbine case. Appropriate non-dimensionalization is given in §3.7. The foundational material given in this sub-section is well-documented in the literature (Glauert, 1935; Lerbs, 1952; Kerwin and Hadler, 2010, e.g.).

Figure 1 illustrates the fundamental assumptions of moderately-loaded propeller theory: (1) the $\mathcal{Z}$ lifting lines have equal angular spacing and identical loading; (2) the lifting lines are straight, radial lines; and (3) each trailing vortex is assumed to be a helix with fixed radius and pitch, where the pitch angle $\beta_v(r_v)$ is related to the wake-aligned inflow angle at the lifting line, $\beta_i(r_c)$.

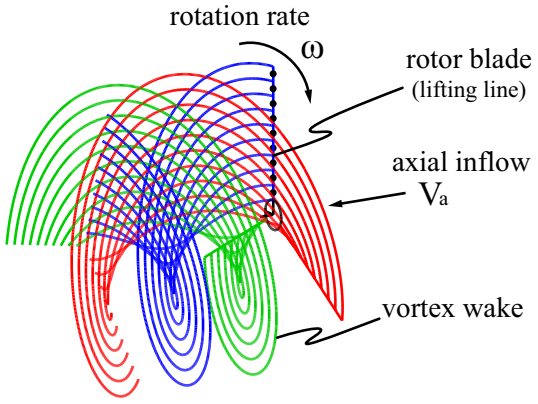

Figure 1: Classical propeller lifting line model, with the control points on the key blade indicated by '•'.

Figure 2 illustrates the velocities and forces (per unit radius) on a blade section: axial and tangential inflow velocities, V_a and V_t; induced velocities, u_a^* and u_t^*; and angular velocity ω. The total resultant inflow velocity has magnitude $V^* = \sqrt{(V_a + u_a^*)^2 + (\omega r + V_t + u_t^*)^2}$ and is oriented at pitch angle β_i to the $\mathbf{e_t}$ direction.

$$\tan\beta_i = \frac{V_a + u_a^*}{\omega r + V_t + u_t^*} \tag{2.1}$$

Also shown on Figure 2 are the angle of attack, α; blade pitch angle, $\theta = \alpha + \beta_i$; circulation, $\Gamma\,\mathbf{e_r}$; inviscid lift, $F_i = \rho V^* \Gamma$; and viscous drag, $F_v = \frac{1}{2}\rho(V^*)^2 C_D c$, given the fluid density ρ, chord c, and drag coefficient C_D. The section lift coefficient is defined as

$$C_L \equiv \frac{F_i}{\frac{1}{2}\rho(V^*)^2 c} = \frac{2\,\Gamma}{V^*\,c} \tag{2.2}$$

The thrust and torque acting on the rotor are

$$\mathbf{T} = \mathcal{Z}\int_{R_h}^{R} [F_i\cos\beta_i - F_v\sin\beta_i]\,dr \qquad (\mathbf{e_a}) \tag{2.3}$$

$$\mathbf{Q} = \mathcal{Z}\int_{R_h}^{R} [F_i\sin\beta_i + F_v\cos\beta_i]\,r\,dr \qquad (-\mathbf{e_a}) \tag{2.4}$$

where R_h and R are the hub and tip radii.

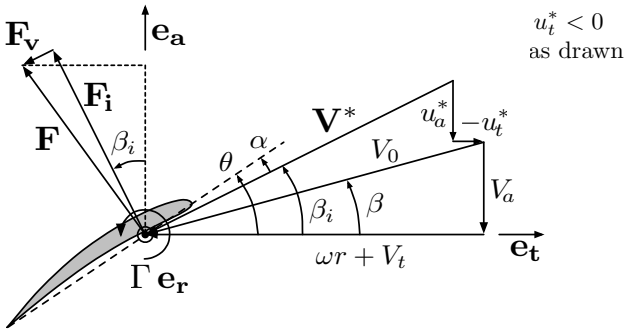

Figure 2: Propeller velocity diagram at radius r.

The power required to drive the propeller is $P = Q\omega$, and The useful power produced by the propeller is TV_s where V_s is the ship speed (i.e. free-stream speed), so the efficiency is

$$\eta = \frac{TV_s}{Q\omega} \tag{2.5}$$

This rotor lifting-line formulation can also describe a horizontal-axis turbine simply by allowing a negative circulation ($\Gamma < 0$) and other associated sign changes. In fact, equations (2.1)-(2.4) are identical to those found in turbine blade element theory (Manwell et al, 2009), allowing for sign and notation differences. Figure 3 shows the turbine velocity/force diagram, with $\{\Gamma,\ F_i,\ u_a^*,\ -u_t^*,\ C_L,\ \alpha,\ T,\ Q,\ P\} < 0$ as drawn. Since these sign changes are automatically handled by the equations given herein, the present lifting-line model unifies both the propeller and turbine cases.

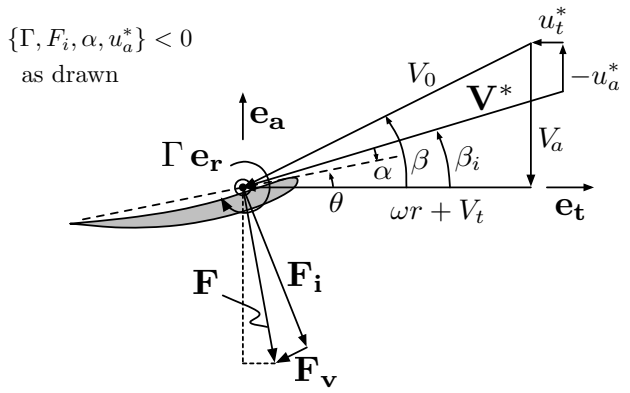

Figure 3: Turbine velocity diagram at radius r.

2.1 Wake model

The wake model consists of constant-pitch, constant-radius helical vortices, whose pitch are aligned with the total velocity at the blade, including induced velocities (i.e. aligned with β_i, as shown in Figure 2).

The induced velocities and loads shown in Figure 2 are computed at control points on the key lifting line at radial locations $r_{c(m)}$, $(m=1...M)$, at the midpoint of each vortex panel. The induced velocities are as follows:

$$u_a^*(m) = \sum_{n=1}^{M} \bar{u}_a^*(m,n)\,\Gamma(n) \tag{2.6}$$

(and similarly for u_t^*), where $\bar{u}_a^*(m,n)$ and $\bar{u}_t^*(m,n)$ are the axial and tangential velocity induced at $r_{c(m)}$ on the key blade by unit-strength 'horseshoe vortices' surrounding the n^{th} panel of each of the $\mathcal{Z}$ blades (where a horseshoe vortex consists of a segment of the lifting line and the trailing vortex filaments shed from its endpoints). The horseshoe influence functions ($\bar{u}_a^*$ and $\bar{u}_t^*$) are in general computed via the Biot-Savard law, but for a purely helical wake, they can be evaluated analytically using the formulas in (Lerbs, 1952) and (Wrench, 1957), which depend on the wake pitch angle.

As described in detail in (Epps, 2013) and illustrated in Figures 4 and 5, the *present* wake model differs from the *classical* model. In the *classical* model, the wake pitch is interpolated from the pitch computed at the control points, which introduces mathematical inconsistencies in the (Lerbs, 1952) and (Wrench, 1957) formulas. The *present* wake model overcomes this difficulty by assuming that each vortex panel has constant pitch and that the pitch angle of the trailing vortices are analytically related to the pitch angle at the control points via $r_{v(n)} \tan\beta_{v(n)} = r_{v(n+1)} \tan\beta_{v(n+1)} = r_{c(n)} \tan\beta_{i(n)}$. This assumption makes the horseshoe influence functions analytically consistent with the pitch at the control points, and thus, it greatly improves the numerical stability and robustness of the rotor lifting line model.

In the classical wake model, one trailing vortex springs from the lifting line at each interior vortex point $r_{v(n=2,...,M)}$, and the strength of this vortex is the difference in the circulation between adjacent vortex panels, $\Gamma_{(n-1)} - \Gamma_{(n)}$. In the present model, *two* vortices are shed at each interior vortex point: The vortex shed from $r_{v(n)}$ with pitch angle $r_{c(n-1)} \tan\beta_{i(n-1)}/r_{v(n)}$ has strength $\Gamma_{(n-1)}$, and the vortex shed with pitch angle $r_{c(n)} \tan\beta_{i(n)}/r_{v(n)}$ has strength $-\Gamma_{(n)}$. In the case that the wake truly is constant-pitch, $r_{c(n-1)} \tan\beta_{i(n-1)} = r_{c(n)} \tan\beta_{i(n)}$ and these two vortices are coincident, as in the classical model. In both models, one trailing vortex springs from each exterior vortex point ($r_{v(n=1)}$ and $r_{v(n=M+1)}$), with strengths $-\Gamma_{(1)}$ and $\Gamma_{(M)}$, respectively.

In reality, the near wake is a continuous vortex sheet, as opposed to a discrete lattice of horseshoe vortices. In modeling this continuous sheet with a discrete number of horseshoes, there is no physical reason to require a single vortex shed from the lifting line at any particular radius: Each constant-strength horseshoe satisfies Helmholtz' Laws independent of the other horseshoes. By setting pitch analytically and allowing the possibility of free vortices with differing pitch as described, the math embodied in the Lerbs/Wrench equations works out to be theoretically consistent with itself. Further details of the present wake model are given in (Epps, 2013).

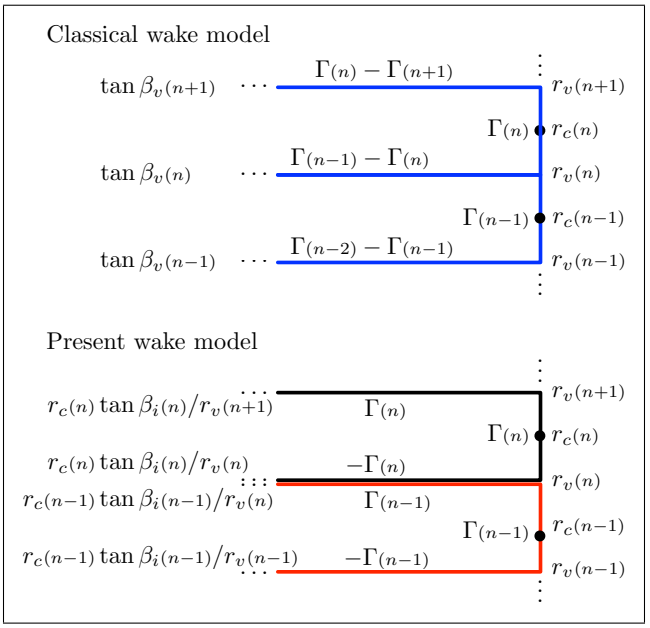

Figure 4: The classical wake model represents a single continuous vortex sheet, whereas the present wake model represents each panel as a constant-pitch vortex sheet (adjacent panels plotted in black and red for clarity).

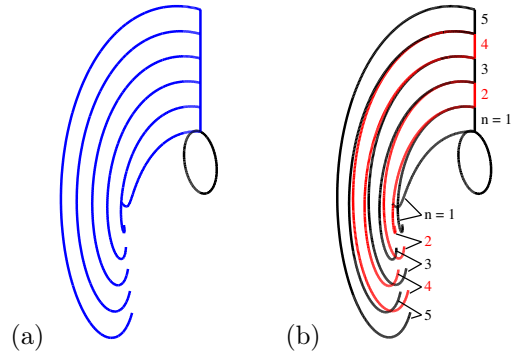

Figure 5: Example illustration of the key blade for the (a) *classical* wake model and (b) *present* wake model (with adjacent panels plotted in black and red for clarity) for a linearly-varying wake pitch: $(r/R)\tan\beta_i(r) = \frac{J}{\pi}\left[0.7 + 0.3\frac{r-R_h}{R-R_h}\right]$.

2.2 Hub and duct modeling

Following (Kerwin and Hadler, 2010), a hub of radius R_h is modeled as an image vortex lattice, where the image trailing vortex filaments have equal and opposite strength as the real vortex filaments and are stationed at radii $r_{h(n,k)} = \frac{R_h^2}{r_{v(n,k)}}$ and have pitch angle $\tan\beta_{h(n,k)} = \frac{r_c(n)\tan\beta_i(n)}{r_h(n,k)}$ where $k = 1, 2$ denotes the edges of the vortex panel (Epps, 2013). The image vorticity is shed through the trailing surface of the hub and rolls up into a *hub vortex* of radius, R_{hv}, and the drag due to the hub vortex is $\mathbf{D_h} = \frac{\rho Z^2}{16\pi}\left[\ln\left(\frac{R_h}{R_{hv}}\right) + 3\right][\Gamma_{(1)}]^2\,(-\mathbf{e_a})$. If a hub image is used in a propeller design, this hub drag is added to the required thrust but does not otherwise alter the optimization equations.

The blade image method can also be applied in the case of a duct to account for the local blade-duct interaction effects during the design process (Kinnas and Coney, 1992). Typically in this case, a thrust ratio is specified, so the rotor is only required to produce a fraction of the total required thrust. The duct itself is modeled as a ring vortex system, which prescribes circulation on the duct to give the intended duct thrust. During each iteration of the design optimization procedure, the duct loading is updated to give the required duct thrust, and the mutual interaction between rotor and duct is recalculated. Details of the duct model are given in (Taylor, 1996) and (Stubblefield, 2008).

Based on the theory in (Kerwin and Hadler, 2010) and the improved wake model in (Epps, 2013), this rotor lifting-line model was coded in the open-source suite `OpenProp 3.0` (Epps and Kimball, 2013), which is used for all calculations herein.

3 Design optimization

The standard propeller design problem is to find the optimum circulation distribution, Γ, for a given inflow (V_a, V_t, ω) and blade outline (c, C_D), such that efficiency is maximized for a prescribed thrust. For the turbine case, the design problem is simply to maximize torque (for the given inflow and blade outline) with no thrust constraint. Since a wake-alignment procedure can be used to determine $\{u_a^*,\ u_t^*,\ \beta_i,\ V^*,\ \bar{u}_a^*,\ \bar{u}_t^*\}$ and ultimately $\{T,Q,\eta\}$ for a given Γ, the circulation distribution serves as a convenient 'parameter system' in the design optimization. That is, both the propeller and turbine design optimization problems reduce to simply finding the optimum circulation distribution.

3.0.1 Simple chord length optimization

Between optimizer iterations, chord lengths may be optimized for drag, structural, or cavitation concerns. A simple method is to set the chord in order to hold the lift coefficient to some maximum allowable value

$$c = \frac{2\,\Gamma}{V^*\,C_{L,\max}} \tag{3.1}$$

in which case the lift coefficient at the design point is $C_{L_0(r)} = C_{L,\max(r)}$ by construction. Many other methods exist in the literature. The present lifting line framework serves as the foundation upon which new methods may be developed and investigated.

3.1 Classical propeller theory

Betz (1919) considered the propeller problem for the case of uniform inflow ($V_a = V_s$) and no viscous forces. Assuming that $\Gamma(r)$ is the optimum circulation distribution, he then added an increment of circulation $\delta\Gamma$ at some arbitrary radius r, causing incremental changes in thrust and torque, δT and δQ. Betz argued that for $\Gamma(r)$ to be optimum, the following 'efficiency' should be independent of radius:

$$\eta^* = \frac{\delta T\,V_s}{\delta Q\,\omega} = \frac{V_s}{\omega r}\frac{\omega r + 2u_t^*}{V_s + 2u_a^*} = \text{constant} \tag{3.2}$$

Assuming $u_a^* \ll V_s$ and $u_t^* \ll \omega r$, one can add higher-order terms to arrive at the 'Betz condition' for optimum free-running propellers

$$\frac{\tan\beta(r)}{\tan\beta_i(r)} = \text{constant} \tag{3.3}$$

Since $\tan\beta(r) = V_s/(\omega r)$, equation (3.3) has the very important implication that $r\tan\beta_i(r) = $ constant, or that the wake forms a constant-pitch helical vortex sheet.

Lerbs (1952) extended the work of Betz to the case of non-uniform axial inflow $V_a(r)$, in which case

$$\begin{aligned}\eta^* &= \frac{\delta T\,V_s}{\delta Q\,\omega} = \frac{V_s}{\omega r}\frac{\omega r + 2u_t^*}{V_a + 2u_a^*} \\ &\approx \frac{V_s}{V_a}\left(\frac{V_a}{\omega r}\right)^2 \frac{(\omega r)^2 + 2u_t^*(\omega r) + (u_t^*)^2}{V_a^2 + 2u_a^* V_a + (u_a^*)^2} = \text{constant}\end{aligned}$$

and thus the optimum propeller satisfies the 'Lerbs criterion':

$$\frac{\tan\beta(r)}{\tan\beta_i(r)} = \text{constant}\cdot\sqrt{\frac{V_a(r)}{V_s}} \tag{3.4}$$

A propeller design code implementing Lerbs criterion (developed by Kerwin (2007)) is used herein as validation for the more advanced Lagrange multiplier methods developed subsequently.

3.2 Lagrange multiplier methods

The propeller optimization problem can also be solved using the 'Lagrange multiplier method'. Kerwin, Coney, and Hsin (1986) have solved this problem for both single- and multi-component propulsors. In the single-component case, they find the set of M vortex panel circulations that produce the least torque for a specified thrust, $T = T_s$. They form an auxiliary function, $H = Q + \lambda_1(T - T_s)$, where λ_1 is a Lagrange multiplier, and they find the optimum Γ by setting the

partial derivatives of H to zero

$$\frac{\partial H}{\partial \Gamma_{(i)}} = 0, \quad \frac{\partial H}{\partial \lambda_1} = 0 \tag{3.5}$$

This is a system of $M+1$ non-linear equations for as many unknowns $\{\Gamma_{(i=1\ldots M)},\ \lambda_1\}$, which can be solved iteratively.

For the turbine case, the design problem is simply to maximize torque, with no thrust constraint

$$\frac{\partial Q}{\partial \Gamma_{(i)}} = 0 \tag{3.6}$$

This is arrived at from (3.5) obviously by setting $\lambda_1 = 0$ and removing the $\frac{\partial H}{\partial \lambda_1} = 0$ equation. Thus, there should exist a single formulation that can be used for both the propeller (3.5) or turbine (3.6) applications.

Rewriting the thrust and torque in terms of the induced velocities and assuming $V_t = 0$ (without loss of generality), equations (2.3) and (2.4) become

$$\frac{T}{\rho \mathcal{Z}} = \sum_{m=1}^{M} \left\{ [\omega r_c + u_t^*]\Gamma - \tfrac{1}{2} V^* C_D c [V_a + u_a^*] \right\} \triangle r_v \tag{3.7}$$

$$\frac{Q}{\rho \mathcal{Z}} = \sum_{m=1}^{M} \left\{ [V_a + u_a^*]\Gamma + \tfrac{1}{2} V^* C_D c [\omega r_c + u_t^*] \right\} r_c \triangle r_v \tag{3.8}$$

The key difficulty of this problem is in how to properly take the derivatives of $\{u_a^*,\, u_t^*,\, V^*\}$ with respect to Γ. We will now show that while the standard approach to these derivatives successfully works for propellers, it does not yield the correct turbine optimization.

3.3 Lifting line approach

In the standard lifting line approach, the partial derivatives of the induced velocities are assumed to be

$$\begin{aligned} \frac{\partial u_a^*{}_{(m)}}{\partial \Gamma_{(i)}} &= \bar{u}_a^*{}_{(m,i)} \\ \frac{\partial u_t^*{}_{(m)}}{\partial \Gamma_{(i)}} &= \bar{u}_t^*{}_{(m,i)} \\ \frac{\partial V^*{}_{(m)}}{\partial \Gamma_{(i)}} &= \sin\beta_{i(m)}\, \bar{u}_a^*{}_{(m,i)} + \cos\beta_{i(m)}\, \bar{u}_t^*{}_{(m,i)} \end{aligned} \tag{3.9}$$

which is consistent with (2.6) and the definition of V^*.

3.3.1 Lifting-line propeller optimization

Using the lifting line assumptions (3.9), the propeller optimization equations (3.5) become

$$\begin{aligned} &(V_{a(i)} + u_a^*{}_{(i)}) r_{c(i)} \triangle r_{v(i)} \\ &+ \sum_m \bar{u}_a^*{}_{(m,i)}\, \Gamma_{(m)} r_{c(m)} \triangle r_{v(m)} \\ &+ \sum_m \tfrac{1}{2} C_{D(m)} c_{(m)} \tfrac{\partial V^*{}_{(m)}}{\partial \Gamma_{(i)}} [\omega r_{c(m)} + u_t^*{}_{(m)}] r_{c(m)} \triangle r_{v(m)} \\ &+ \sum_m \tfrac{1}{2} C_{D(m)} c_{(m)} V^*{}_{(m)} [\bar{u}_t^*{}_{(m,i)}] r_{c(m)} \triangle r_{v(m)} \\ &+ \lambda_1 [\omega r_{c(i)} + u_t^*{}_{(i)}] \triangle r_{v(i)} \\ &+ \lambda_1 \sum_m \bar{u}_t^*{}_{(m,i)}\, \Gamma_{(m)} \triangle r_{v(m)} \\ &- \lambda_1 \sum_m \tfrac{1}{2} C_{D(m)} c_{(m)} \tfrac{\partial V^*{}_{(m)}}{\partial \Gamma_{(i)}} \left[V_{a(m)} + u_a^*{}_{(m)} \right] \triangle r_{v(m)} \\ &- \lambda_1 \sum_m \tfrac{1}{2} C_{D(m)} c_{(m)} V^*{}_{(m)} [\bar{u}_a^*{}_{(m,i)}] \triangle r_{v(m)} \\ &\qquad = 0 \quad \text{for} \quad i = 1 \ldots M \end{aligned}$$

$$\begin{aligned} &\sum_m [\omega\, r_{c(m)} + u_t^*{}_{(m)}] \Gamma_{(m)} \triangle r_{v(m)} \\ &- \sum_m \tfrac{1}{2} C_{D(m)} c_{(m)} V^*{}_{(m)} [V_{a(m)} + u_a^*{}_{(m)}] \triangle r_{v(m)} \\ &\qquad = T_s / (\rho \mathcal{Z}) \end{aligned} \tag{3.10}$$

This system of equations can be solved in a number of ways. Coney (1989) linearizes (3.10) into a system of the form $[A] \cdot [\Gamma; \lambda_1] = [B]$. He then iteratively solves for $\{\Gamma,\ \lambda_1\}$ and then 'aligns the wake' by updating the other parameters $\{u_a^*,\ u_t^*,\ \beta_i,\ \beta_v,\ \bar{u}_a^*,\ \bar{u}_t^*,\ V^*,\ \frac{\partial V}{\partial \Gamma}\}$. Coney's implementation is embodied in the computer code `PLL`.

This linearized solution procedure is tenuous, since it is prone to crash if the induced velocities do not vary smoothly over the span. Epps et al (2009) overcame this difficulty by smoothing the induced velocities at the blade root and tip between each solver iteration. Epps' method is coded in `OpenProp` versions 2.4 and prior.

The present 'LL-Linear' method also iteratively solves a linearized version of (3.10). However, it employs the present wake model, which analytically relates the wake pitch angle β_v to the inflow angle, β_i. By prescribing the correct analytic wake pitch angle, the 'LL-Linear' method is much more robust than its predecessors. In fact, no smoothing of the induced velocities is performed in the 'LL-Linear' method, and it is capable of designing propellers for bollard pull, in which case `PLL` and `OpenProp 2.4` fail.

A possibly more robust approach is to solve (3.10) using a Newton solver. In the 'LL-Newton' formulation developed herein, $\{\Gamma,\, u_a^*,\, u_t^*,\, \tan\beta_i,\, \lambda_1\}$ are taken as the vector of unknowns updated by the Newton solver, and

$\{\bar{u}_a^*,\ \bar{u}_t^*,\ V^*,\ \frac{\partial V}{\partial \Gamma}\}$ are updated between solver iterations.

It is easy to verify that, ignoring viscous effects $C_D = 0$, this propeller optimization method is consistent with the Lerbs criterion (3.4). Using the approximations (3.21) (to appear in §3.5), equations (3.10) imply

$$\lambda_1 \approx -\frac{V_{a(i)} + 2u^*_{a(i)}}{\omega r_{(i)} + 2u^*_{t(i)}} r_{c(i)} \tag{3.11}$$

Since $\lambda_1 =$ constant by definition, it is easy to see that (3.11) implies $\eta^* =$ constant as well, thus satisfying the Lerbs criterion for the propeller.

3.3.2 Lifiting-line turbine optimization

While the lifting line approach embodied in (3.10) yields the proper propeller optimization, it is not applicable to the turbine design problem. The following lifting line turbine optimization system of equations can be arrived at from (3.10) by setting $\lambda_1 = 0$ and removing the thrust constraint, or it may be derived directly from (3.6), (3.8), and (3.9). Either results in this (incorrect) system of turbine optimization equations:

$$\begin{aligned}
&(V_{a(i)} + u^*_{a(i)}) r_{c(i)} \triangle r_{v(i)} \\
&+ \sum_m \bar{u}^*_{a(m,i)}\, \Gamma_{(m)} r_{c(m)} \triangle r_{v(m)} \\
&+ \sum_m \tfrac{1}{2} C_{D(m)} c_{(m)} \tfrac{\partial V^*_{(m)}}{\partial \Gamma_{(i)}} [\omega r_{c(m)} + u^*_{t(m)}] r_{c(m)} \triangle r_{v(m)} \\
&+ \sum_m \tfrac{1}{2} C_{D(m)} c_{(m)} V^*_{(m)} [\bar{u}^*_{t(m,i)}] r_{c(m)} \triangle r_{v(m)} \\
&\qquad = 0 \quad \text{for} \quad i = 1 \ldots M
\end{aligned} \tag{3.12}$$

In the turbine 'LL-Newton' method, equations (3.12) are solved using a Newton solver that employs $\{\Gamma,\ u_a^*,\ u_t^*,\ \beta_i\}$ as the vector of unknowns, with $\{\bar{u}_a^*,\ \bar{u}_t^*,\ V^*,\ \frac{\partial V}{\partial \Gamma}\}$ updated between solver iterations, similar to the propeller 'LL-Newton' method.

Turbines optimized by (3.12) underperform turbine momentum theory. The reason for the shortcomings of this method can be shown by simplifying (3.12) using approximations (3.21) (to appear in §3.5) and $C_D = 0$. In that case, (3.12) results in $u^*_{a(i)} \approx -\frac{1}{2} V_{a(i)}$, which does not agree with classical momentum theory.

This problem has been discovered and addressed by other researchers who have used this method. For example, Kinnas et al (2012) obtain a baseline circulation distribution by solving (3.12) and then search for the optimal solution by scaling their baseline distribution by an arbitrary linear function. Another work-around would be to abandon (3.12) altogether and instead search for the optimum circulation distribution using a genetic algorithm. In lieu of these searching methods, we seek to develop a system of equations that directly yields the optimum circulation distribution.

3.4 Classical turbine momentum theory

Reconsider the turbine optimization problem of maximizing negative torque (and hence, power extraction) for given a turbine radius R, rotation speed ω, and uniform inflow ($V_a = V_s$) with no swirl ($V_t = 0$). In the momentum formulation, the torque is computed via

$$Q = \int_0^R \rho (V_s + \tilde{u}_a)(2\tilde{u}_t) 2\pi r^2 dr \tag{3.13}$$

where $\dot{m} = \rho(V_s + \tilde{u}_a) 2\pi r\, dr$ is the mass flow rate through an annulus of radius r and span dr, $\tilde{u}_a$ and $\tilde{u}_t$ are the circumferential average induced velocities at the propeller disk:

$$\begin{aligned}
\tilde{u}_a(r) &= \frac{\mathcal{Z}}{4\pi r \tan \tilde{\beta}_i(r)} \Gamma(r) \\
\tilde{u}_t(r) &= -\frac{\mathcal{Z}}{4\pi r} \Gamma(r)
\end{aligned} \tag{3.14}$$

(Hough and Ordway, 1964), and $(2\tilde{u}_t)$ is the circumferential average swirl velocity far downstream.

Momentum theory assumes from the outset that the wake forms a constant-radius constant-pitch vortex sheet (Glauert, 1935). This assumption has two main implications: First, it can be shown that in this case the induced velocity is perpendicular to the resultant inflow (Kerwin and Hadler, 2010). That is,

$$(\tan \tilde{\beta}_i \equiv) \quad \frac{V_s + \tilde{u}_a}{\omega r + \tilde{u}_t} = -\frac{\tilde{u}_t}{\tilde{u}_a} \tag{3.15}$$

(Manwell et al, 2009, eqn. (3.25)). This equation can be manipulated as follows to lead to a "design constraint" that is simply a restatement of (3.15):

$$\frac{\partial}{\partial \tilde{u}_t} \left\{ (V_s + \tilde{u}_a)\tilde{u}_a = -(\omega r + \tilde{u}_t)\tilde{u}_t \right\}$$

which leads to the design constraint that appears in classical turbine momentum theory:

$$\frac{\partial \tilde{u}_a}{\partial \tilde{u}_t} = -\frac{\omega r + 2\tilde{u}_t}{V_s + 2\tilde{u}_a} \tag{3.16}$$

Second, the circumferential average velocities (3.14) were derived under the assumptions of constant-radius constant-pitch wake (Hough and Ordway, 1964). The critical feature of these velocities is that they are independent of the circulation at other radii. We will exploit this feature when evaluating the derivatives $\left\{ \frac{\partial u_a^*}{\partial \Gamma}, \frac{\partial u_t^*}{\partial \Gamma}, \frac{\partial V^*}{\partial \Gamma} \right\}$ in §3.5. For now, we continue by noting that this radial independence means that optimization can be performed strip-wise by maximizing $F = (V_s + \tilde{u}_a)\tilde{u}_t$ for each blade section independently. Design optimization is performed by setting $\frac{\partial F}{\partial \tilde{u}_t} = 0$ while

enforcing (3.16). That is,

$$(V_s + \tilde{u}_a) + \left(\frac{\partial \tilde{u}_a}{\partial \tilde{u}_t}\right) \tilde{u}_t = 0 \tag{3.17}$$

Making use of (3.15) and (3.16)

$$(V_s + \tilde{u}_a) + \left(-\frac{\omega r + 2\tilde{u}_t}{V_s + 2\tilde{u}_a}\right) \tilde{u}_t \cdot \left(-\frac{V_s + \tilde{u}_a}{\omega r + \tilde{u}_t}\frac{\tilde{u}_a}{\tilde{u}_t}\right) = 0$$

leads to the resulting optimization equation:

$$\frac{\tilde{u}_t}{\omega r} = -\frac{V_s + 3\tilde{u}_a}{V_s + 4\tilde{u}_a} \tag{3.18}$$

(Manwell et al, 2009, eqn. (3.36)). In the limit $\tilde{u}_t \ll \omega r$, equation (3.18) reduces to $\tilde{u}_a = -\frac{1}{3}V_s$. In this case, the power coefficient becomes $C_P = 16/27$, which is the familiar 'Betz limit'.

Momentum theory can also be applied in the viscous case, assuming a constant drag to lift ratio $\frac{C_D}{C_L}$ and uniform wind V_s (Stewart, 1976). In his derivation, Stewart (1976) uses the wake pitch angle $\tilde{\beta}_i$ as the independent variable, maximizing power extraction while enforcing (3.15) to arrive at

$$\frac{V_s}{-\tilde{u}_a} = 2 + \frac{\frac{C_D}{C_L}\sec^2\tilde{\beta}_i}{2\left(\tan\tilde{\beta}_i - \frac{C_D}{C_L}\right)} + \sec\tilde{\beta}_i \left[\frac{\tan\tilde{\beta}_i}{\left(\tan\tilde{\beta}_i - \frac{C_D}{C_L}\right)} + \frac{\left(\frac{C_D}{C_L}\right)^2 \sec^2\tilde{\beta}_i}{4\left(\tan\tilde{\beta}_i - \frac{C_D}{C_L}\right)^2}\right]^{\frac{1}{2}} \tag{3.19}$$

which reduces to (3.18) in the inviscid case.

Equations (3.15) and (3.19) can be used to form a table of optimum $\tilde{u}_a$ and $\tilde{u}_t$ versus $\omega r/V_s$, and equation (3.14) can the be used to find the blade loading, Γ. However, these results suffer a few limitations. First, equation (3.14) is only valid in the limit of an infinite number of blades. For a 3-bladed turbine, say, a 'circulation reduction factor' (a.k.a. the 'Prandtl tip factor') must be included in (3.14). The lifting line wake model automatically accounts for this circulation reduction factor. Second, this momentum method does not natively handle features such as a hub or duct, which again are automatically handled in the lifting line model. Finally, this formulation is limited to the assumption that C_D/C_L is constant. Since C_D actually is constant for a family of airfoils with varying camber, assuming C_D/C_L is constant implicitly assumes chord length optimization to hold C_L constant as well. In practical design, the blade outline may be chosen for structural reasons, in which case this method fails. Thus, it is preferable to employ lifting line theory natively in the turbine optimization.

3.5 Hybrid approach

Momentum theory considerations are now used to formulate a hybrid lifting-line/momentum-theory optimization procedure. This results in a procedure that is capable of optimizing both propellers and turbines using the same code! As with classical turbine momentum theory, the restriction is that this method is only valid in the case of uniform inflow: $V_a(r) = V_s$.

In creating this 'Hybrid' method, we seek to preserve two salient features of momentum theory: First, momentum theory provides the 'design constraint' (3.16), which implicitly enforces the wake to be constant-pitch, as desired in the uniform-inflow case. In the discrete lifting-line formulation, equation (3.16) becomes

$$\frac{\partial u^*_{a(i)}}{\partial u^*_{t(i)}} = -\frac{\omega r_{c(i)} + 2u^*_{t(i)}}{V_s + 2u^*_{a(i)}} \tag{3.20}$$

which is the general turbine design constraint. The problem now is how to incorporate this constraint into the lifting line optimization equations (3.5) or (3.6). This is accomplished in the way that the partial derivatives $\left\{\frac{\partial u^*_a}{\partial \Gamma}, \frac{\partial u^*_t}{\partial \Gamma}, \frac{\partial V^*}{\partial \Gamma}\right\}$ are evaluated.

The second salient feature of momentum theory is that the induced velocities are independent of the circulation at other radii. This is actually recovered in the lifting line formulation in the limit of a large number of blades (which is not surprising, since the actuator disk model used in momentum theory simply is the limit of an infinite number of infinitesimally-loaded lifting lines). Consider the horseshoe influence functions used in the lifting line model, $\bar{u}^*_a$ and $\bar{u}^*_t$. Careful examination of the equations in (Lerbs, 1952) shows that for a large number of blades, the horseshoe influence matrices are nearly diagonal. That is, for a large number of blades, one can reasonably make the approximations

$$\begin{aligned} \bar{u}^*_{a(m,i)} &\approx 0 \qquad (\text{for } m \neq i) \\ \bar{u}^*_{t(m,i)} &\approx 0 \qquad (\text{for } m \neq i) \\ u^*_{a(i)} &\approx \bar{u}^*_{a(i,i)}\,\Gamma_{(i)} \\ u^*_{t(i)} &\approx \bar{u}^*_{t(i,i)}\,\Gamma_{(i)} \end{aligned} \tag{3.21}$$

In the limit of an infinite-bladed rotor (i.e. an actuator disk), the off-diagonal terms become zero and equations (3.21) become exact. Practically, $\mathcal{Z} > 50$ blades yields this result to $O(10^{-5})$ for any reasonably fine discretization (say $M > 10$ panels).

Furthermore, in the infinite-bladed case, the circumferentially-varying component of the (Lerbs, 1952) equations is zero, so the induced velocities (2.6) are equal to the circumferential average velocities (3.14). As a point of inter-model consistency, Epps (2013) shows that the lifting line model must include the assumption of locally-constant-pitch wake horseshoes such that (2.6) and (3.14) are indeed equal in the infinite-bladed case.

This modeling assumption is required in the turbine application in order to recover the classical actuator disk results for power coefficient versus tip speed ratio.

Momentum theory equations (3.14) along with lifting line approximations (3.21) lead to the following set of hybrid assumptions: For $m = i$,

$$\frac{\partial u_a^*(m)}{\partial \Gamma_{(i)}} \quad \left(= \frac{\partial u_a^*(m)}{\partial u_t^*(m)} \frac{\partial u_t^*(m)}{\partial \Gamma(i)}\right) = \frac{\partial u_a^*(i)}{\partial u_t^*(i)} \bar{u}_{t\,(i,i)}^* \quad (3.22a)$$

$$\frac{\partial u_t^*(m)}{\partial \Gamma_{(i)}} = \bar{u}_{t\,(i,i)}^* \quad (3.22b)$$

$$\frac{\partial u_a^*(m)}{\partial \Gamma_{(i)}} \Gamma_{(m)} \left(= \frac{\partial u_a^*(m)}{\partial u_t^*(m)} \frac{\partial u_t^*(m)}{\partial \Gamma(i)} \Gamma_{(m)}\right) = \frac{\partial u_a^*(i)}{\partial u_t^*(i)} u_{t\,(i)}^* \quad (3.22c)$$

$$\frac{\partial u_t^*(m)}{\partial \Gamma_{(i)}} \Gamma_{(m)} = u_{t\,(i)}^* \quad (3.22d)$$

$$\frac{\partial V^*(m)}{\partial \Gamma_{(i)}} = \left(\sin\beta_{i(i)} \frac{\partial u_a^*(i)}{\partial u_t^*(i)} + \cos\beta_{i(i)}\right) \bar{u}_{t\,(i,i)}^* \quad (3.22e)$$

and each is taken as 0 for $m \neq i$. Recall, the derivative $\frac{\partial u_a^*(i)}{\partial u_t^*(i)}$ is evaluated using (3.20). Equations (3.22a), (3.22c), and (3.22e) are simple applications of the chain rule of calculus, with their final forms having made use of equations (3.22b) and (3.22d). Equations (3.22b) and (3.22d) are analytically consistent with (3.14) for a large number of blades.

The essential feature of momentum theory, which is readily obvious in (3.15) but is buried in the derivations of (3.14) and (3.16), is the assumption that the induced velocity is perpendicular to the inflow. Essentially what equations (3.20) and (3.22) do is constrain the lifting line method to achieve the same flow perpendicularity that is built into the momentum model

$$(\tan\beta_i \equiv) \quad \frac{V_s + u_a^*}{\omega r + u_t^*} \approx -\frac{u_t^*}{u_a^*}$$

regardless of the number of blades. Equations (3.20) and (3.22) are analogous to the Betz condition for propeller optimization (3.3), which enforces flow perpendicularity in the propeller design case (again regardless of the number of blades). Since 'Hybrid' equations (3.20) and (3.22) enforce the Betz condition (3.3) of constant pitch wake, the 'Hybrid' method is only valid in the uniform inflow case.

3.5.1 Hybrid propeller optimization

Using these assumptions, the system of equations for the propeller design optimization problem (3.5) becomes

$$\begin{aligned}
&(V_s + u_{a\,(i)}^*) r_{c(i)} \\
&+ \tfrac{\partial u_a^*(i)}{\partial u_t^*(i)} u_{t\,(i)}^* r_{c(i)} \\
&+ \tfrac{1}{2} C_{D(i)} c_{(i)} \tfrac{\partial V^*(i)}{\partial \Gamma(i)} [\omega r_{c(i)} + u_{t\,(i)}^*] r_{c(i)} \\
&+ \tfrac{1}{2} C_{D(i)} c_{(i)} V^*{}_{(i)} [\bar{u}_{t\,(i,i)}^*] r_{c(i)} \\
&+ \lambda_1 [\omega r_{c(i)} + u_{t\,(i)}^*] \\
&+ \lambda_1 u_{t\,(i)}^* \\
&- \lambda_1 \tfrac{1}{2} C_{D(i)} c_{(i)} \tfrac{\partial V^*(i)}{\partial \Gamma(i)} \left[V_s + u_{a\,(i)}^*\right] \\
&- \lambda_1 \tfrac{1}{2} C_{D(i)} c_{(i)} V^*{}_{(i)} [\bar{u}_{a\,(i,i)}^*] \\
&\qquad = 0 \quad \text{for} \quad i = 1 \ldots M
\end{aligned}$$

$$\begin{aligned}
&\sum_m [\omega\, r_{c(m)} + u_{t\,(m)}^*] \Gamma_{(m)} \triangle r_{v(m)} \\
&- \sum_m \tfrac{1}{2} C_{D(m)} c_{(m)} V^*{}_{(m)} [V_s + u_{a\,(m)}^*] \triangle r_{v(m)} \\
&\qquad = T_s / (\rho \mathcal{Z})
\end{aligned} \quad (3.23)$$

The 'Hybrid' propeller optimization method solves (3.23) using a Newton solver.

In the inviscid case, (3.23) yields

$$\begin{aligned}
-\frac{\lambda_1}{r_{c(i)}} &\approx \frac{V_s + u_{a\,(i)}^* + \frac{\partial u_a^*(i)}{\partial u_t^*(i)} u_{t\,(i)}^*}{\omega r_{(i)} + 2 u_{t\,(i)}^*} \\
&\approx \frac{V_s + 2 u_{a\,(i)}^*}{\omega r_{(i)} + 2 u_{t\,(i)}^*} - \frac{u_{a\,(i)}^*}{\omega r_{(i)} + 2 u_{t\,(i)}^*} - \frac{u_{t\,(i)}^*}{V_s + 2 u_{a\,(i)}^*}
\end{aligned} \quad (3.24)$$

which, to the leading order is consistent with Betz condition for the propeller (3.3).

3.5.2 Hybrid turbine optimization

The analogous system of equations for the turbine is

$$\begin{aligned}
&(V_s + u_{a\,(i)}^*) \\
&+ \tfrac{\partial u_a^*(i)}{\partial u_t^*(i)} u_{t\,(i)}^* \\
&+ \tfrac{1}{2} C_{D(i)} c_{(i)} \tfrac{\partial V^*(i)}{\partial \Gamma(i)} [\omega r_{c(i)} + u_{t\,(i)}^*] \\
&+ \tfrac{1}{2} C_{D(i)} c_{(i)} V^*{}_{(i)} [\bar{u}_{t\,(i,i)}^*] \\
&\qquad = 0 \quad \text{for} \quad i = 1 \ldots M
\end{aligned} \quad (3.25)$$

Equation (3.25) can be arrived at from (3.23) by setting $\lambda_1 = 0$ and removing the thrust constraint, or it may be derived directly from (3.6), (3.8), (3.20), and (3.22). Momentum theory for the inviscid case (3.17) is directly recovered from (3.25). The 'Hybrid' turbine optimization method solves (3.25) using a Newton solver. This is actually implemented in the same code as the 'Hybrid' propeller method, with $\lambda_1 = 0$ and the thrust constraint equation removed.

3.5.3 Robust turbine optimization

As part of this investigation, several numerical implementations of system (3.25) were studied to determine if anything could be done to enhance the stability and robustness of the code. Although details of these numerical studies will not be presented, it is worth noting that one much more robust numerical implementation was found. This version of system (3.25) is formed by multiplying each equation by $(V_s + 2u^*_{a(i)})$ to arrive at

$$\begin{aligned}
&(V_s + 2u^*_{a(i)})(V_s + u^*_{a(i)}) \\
&- (\omega r_{c(i)} + 2u^*_{t(i)})(u^*_{t(i)}) \\
&+ (V_s + 2u^*_{a(i)})\tfrac{1}{2}C_{D(i)}c_{(i)}\frac{\partial V^*_{(i)}}{\partial \Gamma_{(i)}}[\omega r_{c(i)} + u^*_{t(i)}] \\
&+ (V_s + 2u^*_{a(i)})\tfrac{1}{2}C_{D(i)}c_{(i)}V^*_{(i)}[\bar{u}^*_{t(i,i)}] \\
&\qquad = 0 \quad \text{for} \quad i = 1 \ldots M
\end{aligned} \tag{3.26}$$

This is embodied in the 'Robust' turbine method, which solves (3.26) using a Newton solver. This was found to be the most stable and robust turbine optimization code that was able to replicate momentum theory. One can see readily that for $C_D = 0$ and $u^*_t \ll V_s$, (3.26) implies $u^*_a \approx -\frac{1}{3}V_s$, which is consistent with momentum theory.

As with the 'Hybrid' turbine optimization method (3.25), the 'Robust' turbine optimization method (3.26) is restricted to the case of uniform inflow: $V_a(r) = V_s$.

3.5.4 A note on the uniform inflow restriction

Note that the axial inflow speed $V_a(r)$ has been changed to V_s in optimization equations (3.23), (3.24), (3.25), and (3.26) to explicitly remind the reader that the 'Hybrid' and 'Robust' optimization methods are only valid in the uniform inflow case: $V_a(r) = V_s$.

The assumptions that lead to this uniform flow restriction are quite subtle and will be summarized here: Equations (3.15) and (3.16) are true if and only if the induced velocity is perpendicular to the total inflow velocity. Equations (3.14) and (3.3) are true if and only if the wake is constant pitch. It can be shown that the induced velocity is perpendicular to the inflow (3.15) if and only if the wake is constant pitch (3.3) (Kerwin and Hadler, 2010).

Momentum theory derivations often start by assuming that the induced velocity is perpendicular to the inflow (3.15). Recall, this assumption implies that the wake is constant pitch (3.3). The 'Hybrid' and 'Robust' methods follow the momentum theory assumptions that (3.14)-(3.16) are true; these lead to 'Hybrid' method assumptions (3.20)-(3.22), which ultimately lead to the optimization equations (3.23)-(3.26). Thus, any rotor optimized using the 'Hybrid' method will effectively enforce a constant pitch wake (3.3), regardless of whether the inflow is uniform or not.

In the uniform inflow case, enforcing the Betz condition (3.3) yields the optimum propeller. However, in the non-uniform inflow case, a propeller should be optimized such that the Lerbs criterion (3.4) is true, not the Betz condition (3.3). Thus, the 'Hybrid' method fails in the case of propeller design for non-uniform inflow.

This failure calls into question the validity of the 'Hybrid' method for turbine optimization in the non-uniform inflow case. Given that the 'Hybrid' method is invalid for propeller optimization in non-uniform inflow, it stands to reason that the 'Hybrid' method also is invalid for turbine optimization in non-uniform inflow. The authors have no knowledge of an extended momentum theory for the optimization of turbines in non-uniform inflow, and it seems that turbine optimization using momentum theory always assumes uniform inflow (Manwell et al, 2009; Burton et al, 2001; Hansen, 2008, e.g.).

Determining a general turbine optimization method for non-uniform inflow remains ongoing work. As stated above, one means of accomplishing this would be a genetic algorithm to find the optimum circulation distribution. Alternatively, the method might be to search for the optimum wake pitch distribution (perhaps starting with the constant pitch distribution produced by the 'Robust' method, and then perturbing that pitch distribution iteratively).

In publicly-released versions of `OpenProp v3`, propeller design optimization is achieved via either the 'LL-Linear' or 'LL-Newton' methods, which both admit non-uniform inflow and both solvers yield the same converged results (the difference being a tradeoff between computational speed and stability). Turbine optimization is achieved via the 'Robust' method, which is restricted to the uniform inflow case.

3.6 Summary of methods

The following table summarizes the models and numerical methods developed herein.

Table 1: Summary of design optimization methods (where 'LL' stands for 'Lifting Line', and 'Mom. Theory' stands for momentum theory). The 'Lerbs', 'LL-Linear', 'LL-Newton', 'Hybrid', and 'Robust' methods were implemented in the `OpenProp v3.0` numerical design code (Epps and Kimball, 2013).

Name	Wake model	Opt. eqn.	Numerical method
Propeller methods			
'Lerbs'	Classical	(3.4)	Linear system
'PLL'	Classical	(3.10)	Linear system
'OpenProp v2.4'	Classical	(3.10)	Linear system
'LL-Linear'	Present	(3.10)	Linear system
'LL-Newton'	Present	(3.10)	Newton solver
'Hybrid'	Present	(3.23)	Newton solver
Turbine methods			
'Mom. Theory'	n/a	(3.19)	Analytic
'LL-Newton'	Present	(3.12)	Newton solver
'Hybrid'	Present	(3.25)	Newton solver
'Robust'	Present	(3.26)	Newton solver

The differences in the propeller optimization methods are subtle. Both `PLL` and `OpenProp v2.4` employ the vortex-lattice-based optimization equations (3.10), and they only differ from 'LL-Linear' in their wake models. 'LL-Newton' employs the same wake model and optimization equations as 'LL-Linear', but it is formulated as a Newton solver for better numerical stability. The 'Hybrid' propeller method is based on the hybrid set of optimization equations (3.23), which were developed in §3.5.

For numerical stability, all turbine codes developed herein employ the Newton solver formulation. The 'LL-Newton' turbine code is (of course) the turbine analog of the 'LL-Newton' propeller code, and similarly, the 'Hybrid' turbine code is the turbine analog of the 'Hybrid' propeller code. Finally, the 'Robust' method is analytically-equivalent to the 'Hybrid' turbine method, but it is a much more robust formulation.

In completing this work, the first author considered several additional permutations of these methods, such as the propeller analog of the 'Robust' turbine code, or not including $\tan\beta_i$ in the Newton solver. Also, an alternative set of hybrid assumptions is discussed in Appendix A. Unfortunately, these permutations either resulted in codes with reduced numerical stability or codes that did not converge to physically realistic results. The methods listed in Table 1 represent the best of the many implementations considered by the author.

The first author has implemented the 'LL-Linear' and 'LL-Newton' propeller optimization methods and the 'Robust' turbine optimization methods in `OpenProp` versions 3.0 and beyond. While the 'Hybrid' method successfully demonstrates the link between the propeller and turbine theories, it is not as numerically robust as these other methods.

3.7 Non-dimensionalization

The equations above were derived in dimensional form, as the customary means of non-dimensionalization differ between propeller and turbine theory. The non-dimensionalization employed herein, which is largely taken from propeller theory is as follows. Given a dimensionally-consistent set of fluid density ρ, reference speed V_s, rotor radius R (and diameter $D = 2R$), the other flow parameters are non-dimensionalized as follows. All velocities are normalized by V_s, radii by R, chord lengths by D, and

$$J_s = \frac{V_s}{nD} \qquad \text{(advance coefficient)} \quad (3.27)$$

$$\lambda = \frac{\omega R}{V_s} = \frac{\pi}{J_s} \qquad \text{(tip-speed ratio)} \quad (3.28)$$

$$K_T = \frac{T}{\rho n^2 D^4} \qquad \text{(thrust coefficient)} \quad (3.29)$$

$$K_Q = \frac{Q}{\rho n^2 D^5} \qquad \text{(torque coefficient)} \quad (3.30)$$

$$C_T = \frac{T}{\frac{1}{2}\rho V_s^2 \pi R^2} \qquad \text{(thrust coefficient)} \quad (3.31)$$

$$C_Q = \frac{Q}{\frac{1}{2}\rho V_s^2 \pi R^2} \qquad \text{(torque coefficient)} \quad (3.32)$$

$$C_P = \frac{\omega Q}{\frac{1}{2}\rho V_s^3 \pi R^2} = \lambda C_Q \qquad \text{(power coefficient)} \quad (3.33)$$

$$G = \frac{\Gamma}{2\pi R V_s} \qquad \text{(circulation)} \quad (3.34)$$

where the rotation speed is n (rev/s) or $\omega = 2\pi n$ (rad/s).

4 Optimization examples and validation

4.1 Propeller parametric design study

As an example parametric design study, several hubless, five-bladed propellers are designed to give the same thrust coefficient, $C_T = 0.512$, for a range of advance coefficients. In this example, $V_a(r)/V_s = 1$, $V_t(r) = 0$, and $M = 40$. Circulation was optimized using each of the methods listed in Table 1 for both the inviscid and viscous cases. In the inviscid case ($C_D = 0$), chord lengths are optimized for each propeller with $C_{L,\max(r)} = 0.2$. In the viscous case, we assumed $C_D = 0.008$ and used the blade outline given in Table 2.

Table 2: Blade outline used for viscous study.

r/R	0.2000	0.3000	0.4000	0.5000	0.6000	0.7000
c/D	0.2002	0.2274	0.2531	0.2743	0.2878	0.2913
r/R	0.8000	0.9000	0.9500	0.9750	0.9875	1.0000
c/D	0.2817	0.2410	0.1962	0.1480	0.0988	0.0259

Figure 6 shows the results of this parametric study. The dashed upper limit $\eta_i = 0.8970$ is the ideal efficiency given by 1D momentum (actuator disk) theory,

$$\eta_i = \frac{2}{1 + \sqrt{1 + C_T}} \tag{4.1}$$

This efficiency is indeed reached in the limit $J_s \to 0$ in the inviscid case (upper curves). In the viscous case (lower curves), efficiency approaches zero in the limit $J_s \to 0$, as expected. In the limit $J_s \gg 1$, results for the inviscid and viscous cases converge, which provides a third check.

Qualitatively, the results in Fig. 6 are representative of a typical parametric study with all parameters fixed except for rotation rate. The advance coefficient J_s reaches zero in the limit of infinite rotation rate, in which case the blades are conceptually smeared into an actuator disk. In the inviscid case, $\eta \to \eta_i$ as $J_s \to 0$ for all propeller optimizers, as expected (see Fig. 6(a)). The circulation distribution is nearly constant (Fig. 6(b)), which is consistent with actuator disk theory. On the other hand, as J_s increases, ω decreases, and the circulation increases to maintain the same thrust. This increase in circulation brings about an increase in torque, which decreases the efficiency of the propeller, as reflected in Fig. 6(a).

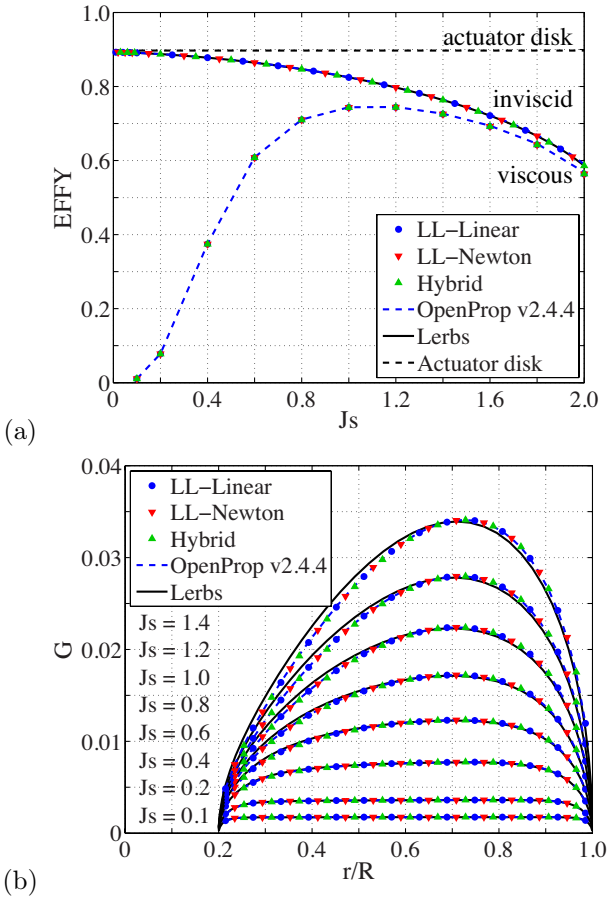

Figure 6: (a) Efficiency and (b) circulation of 5-bladed propellers optimized for each advance coefficient as shown. Circulation results are from the inviscid case. The latter four design methods listed in Table 1 show perfect agreement, and they also compare favorably to the 'Lerbs criterion' based method.

Figure 6 shows that all four Lagrange multiplier methods programmed by the author agree, namely: '`OpenProp v2.4`', 'LL-Linear', 'LL-Newton' , and 'Hybrid'. Comparing '`OpenProp v2.4`' with 'LL-Linear' shows that the choice of wake model has little effect on the propeller design results; the major effect of the present wake model is to improve numerical stability, such that propeller design may be performed without artificially "repairing" the induced velocities, as is done in '`OpenProp v2.4`' (Epps, 2010b). Comparing 'LL-Linear' with 'LL-Newton' shows that the choice of numerical solution method has no effect on the converged design results, thus validating the numerical methods. Comparing 'LL-Newton' with 'Hybrid' shows that the hybrid design optimization method developed in §3.5 yields correctly-optimized propellers. This validates the hybrid method in the propeller case.

Since this example is for a propeller in uniform inflow, the Lerbs criterion (3.4) theoretically yields the optimum propeller efficiency in the inviscid case. Figure 6 shows

that while the Lagrange multiplier methods all yield circulation distributions slightly favoring the tip (as compared to the Lerbs circulation distributions), the computed efficiencies are in close agreement with the Lerbs theoretical maximum.

The original intent of this example was to compare the results in Figure 6 with the 'PLL' results reported in (Coney, 1989, Figs. 2.4 and 2.5). However, for this example, Coney computed the horseshoe influence functions using the lightly-loaded approximation ($\beta_{wake} = \beta$), whereas moderately-loaded theory ($\beta_{wake} = \beta_i$) was employed to create Figure 6. Thus, the 'Lerbs' and 'LL-Linear' codes were run again, this time employing the lightly-loaded model, and these results are shown in Figure 7. This figure shows nearly perfect agreement between the circulation predicted by 'LL-Linear' and 'PLL'. Perfect agreement is also observed in the efficiencies, so these data are not shown. This provides validation of the present methods versus the industry standard code, 'PLL'.

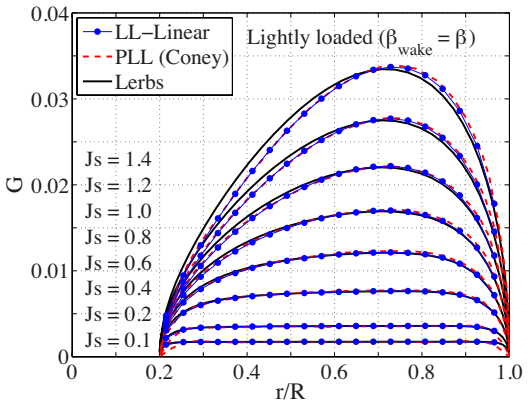

Figure 7: Circulation of 5-bladed propellers optimized for each advance coefficient (assuming inviscid and 'lightly-loaded'), showing nearly perfect agreement between 'LL-Linear' and 'PLL'.

4.2 Turbine parametric design study

Turning our attention to the horizontal-axis turbine application, we now consider a parametric design study in which several turbines are designed to maximize power extraction for a range of tip-speed ratios. In this example, we consider both infinite-bladed ($\mathcal{Z} = 100$) and finite-bladed ($\mathcal{Z} = 3$) cases, assuming uniform inflow ($V_a/V_s = 1$, $V_t = 0$), $M = 80$ panels, inviscid flow ($C_D = 0$), and a blade root radius of $R_{hub}/R = 0.1$. No hub image is used in this study.

Figure 8 shows power coefficient versus tip-speed ratio for each of the turbines designed in the inviscid, infinite-bladed case. Momentum theory is shown as the solid line, and the well-known Betz Limit of $C_P = 16/27 \approx 0.5926$ is reached in the limit of infinite tip speed ratio. Each of the three turbine optimization methods were employed in this study, and good agreement is observed between the 'Hybrid' and 'Robust' methods. The power coefficients computed by the 'Hybrid' and 'Robust' methods nearly replicate momentum theory; the small discrepancy is due to the finite root radius ($R_{hub}/R = 0.1$), which was necessary for numerical stability of the 'Hybrid' and 'LL-Newton' codes.

Taken together, Figures 6 and 8 demonstrate that the 'Hybrid' method is capable of optimizing both propellers and turbines. Thus, the 'Hybrid' method provides the link between propeller lifting line theory and turbine momentum theory.

Figure 8 also shows that while both the 'Hybrid' and 'Robust' methods replicate momentum theory, the turbines designed using the vortex-lattice-based 'LL-Newton' method have noticeably lower power coefficients. The reason for this deficiency is illustrated in Figure 9, which shows the circulation and induced velocities for two turbines designed with $\lambda = 6$, $C_D = 0$, and blade number $\mathcal{Z}$ as shown. For $\mathcal{Z} = 100$, the 'Hybrid' and 'Robust' methods agree with momentum theory, as expected.

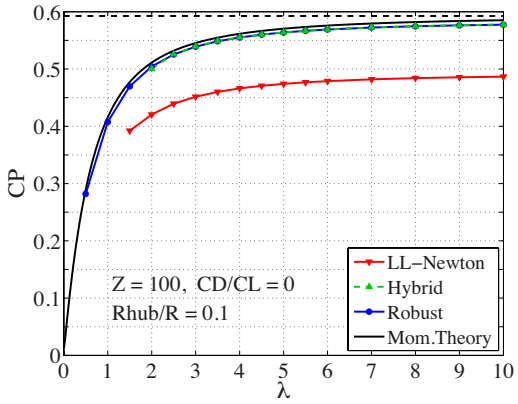

Figure 8: Power coefficient for turbines optimized for each tip speed ratio, with $\mathcal{Z} = 100$, $R_{hub}/R = 0.1$, and $C_D = 0$. The 'Hybrid' and 'Robust' methods agree with momentum theory, whereas the 'LL-Newton' method under-performs the others.

Figure 9b shows that contrary to momentum theory, the 'LL-Newton' method results in $u_a^*/V_s \approx -\frac{1}{2}$. It is well-known from actuator disk theory that the optimal axial induction is $u_a^*/V_s \approx -\frac{1}{3}$, which strikes the optimal balance between allowing mass to flow through the disk and extracting power from this mass. Physically speaking, while an axial induction of $u_a^*/V_s \approx -\frac{1}{2}$ extracts more power per unit mass than $u_a^*/V_s \approx -\frac{1}{3}$, this higher induction reduces the mass flow rate through the disk, thereby decreasing overall power extraction. That equations (3.12) result in $u_a^*/V_s \approx -\frac{1}{2}$ is readily apparent in the infinite-bladed case, since then approximations (3.21) become exact and the result follows. Thus, it is now evident why traditional vortex-

lattice-based turbine optimization yields deficient power coefficients.

Results for the finite-bladed case ($\mathcal{Z} = 3$) are also shown in Figure 9. With $\mathcal{Z} = 3$, the 'Robust' code yields nearly the same induced velocities as the $\mathcal{Z} = 100$ case, but the circulation is now altered to produce these induced velocities with the finite number of blades. Thus, these optimization methods are actually optimizing induced velocity, and the circulation distribution just serves as a convenient independent variable in the derivation of the equations.

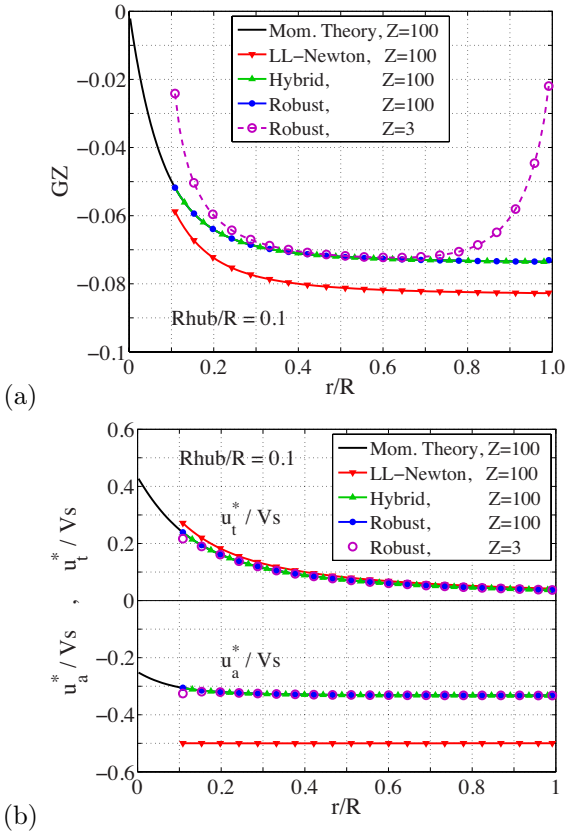

Figure 9: (a) Circulation and (b) induced velocities versus radius for a turbine designed with $\lambda = 6$, $C_D = 0$, $R_{hub}/R = 0.1$ (but no hub image), and blade number as shown.

The effects of blade number and viscous losses are shown in Figure 10. Again, we consider both infinite-bladed ($\mathcal{Z} = 100$) and finite-bladed ($\mathcal{Z} = 3$) cases, and we assume $V_a/V_s = 1$, $V_t = 0$, $M = 80$, and no hub image. Here, we consider both the inviscid case ($C_D = 0$), as well as viscous cases assuming $C_D/C_L = 0.01$ or 0.02, as shown. In the viscous cases, chord is adjusted each iteration to hold C_L constant via (2.2). In order to better match with momentum theory (which assumes zero hub radius), we set $R_{hub}/R = 0.005$.

Figure 10 shows very good agreement between the 'Robust' method and momentum theory for the three drag coefficients shown. For finite drag coefficient, there is an optimum tip speed ratio for which power coefficient is maximized. For finite blade number, the power coefficient is always lower than the infinite bladed case. In the limit $\lambda \to \infty$, the $\mathcal{Z} = 3$ results converge with the $\mathcal{Z} = 100$ results, as expected.

Since the codes developed herein are based on the rotor lifting line model, the required blade circulation is computed for each case, regardless of blade number or drag coefficient, with no circulation reduction factor needed. This allows for seamless design and analysis of optimized horizontal axis turbines.

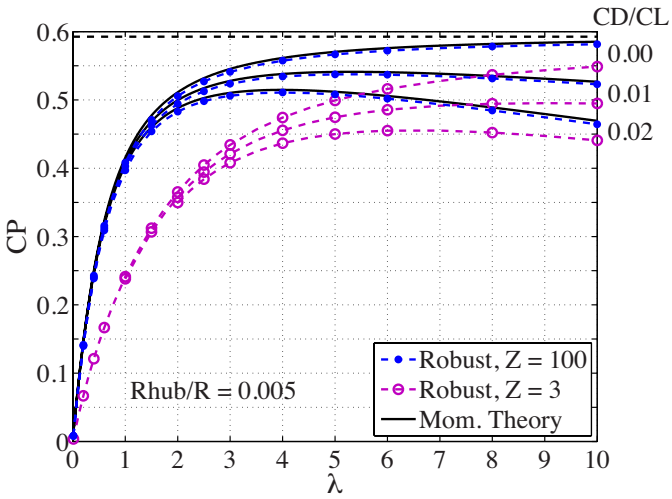

Figure 10: Power coefficient for turbines optimized for each tip speed ratio using the 'Robust' method, with $R_{hub}/R = 0.005$, $M = 80$, and uniform inflow, with $\mathcal{Z}$ and C_D/C_L as shown. Upper curves for $\mathcal{Z} = 100$ agree with momentum theory (solid line), and corresponding lower curves for $\mathcal{Z} = 3$ show the effect of blade number.

5 Rotor geometry and analysis

The rotor design procedure results in a converged set of $\{\Gamma_0,\, V_0^*,\, u_{a_0}^*,\, u_{t_0}^*,\, \beta_{i_0},\, \bar{u}_{a_0}^*,\, \bar{u}_{t_0}^*,\, C_{L_0},\, C_{D_0},\, c\}$, where the subscript 0 denotes the design point. From here, the 3D blade geometry can be determined (see §5.1 and §5.2), or the off-design performance can be analyzed (see §5.3). Note that since C_{L_0} and β_{i_0} are known for the design condition, the blade geometry does not need to be determined to analyze the off-design performance. The only assumption required for the off-design performance analysis is that $C_L = C_{L_0}$ when $\beta_i = \beta_{i_0}$.

5.1 Rotor blade geometry

Typically in the rotor design process, a lifting surface or panel method code is used to determine the full 3D blade geometry that is required to produce the radial load distribution determined by the lifting line optimization algorithm. Another input to the blade design procedure is a starting geometry, which can be estimated from the lifting line model as follows. In §5.2, lifting surface geometry corrections are offered for the propeller case, such that a more accurate starting geometry can be estimated.

The lifting line model assumes that the full 3D rotor geometry is built from 2D section profiles that are scaled and rotated according to the chord length and the design-point lift coefficient and inflow angle $\{c, C_{L_0}, \beta_{i_0}\}$. The camber scaling is such that the ideal lift coefficient of the section equals desired lift coefficient, and the (pitch) rotation is such that the angle of attack is set to the ideal angle of attack. Employing the ideal angle of attack provides shock-free loading, prevents leading edge flow separation, and mitigates cavitation inception.

A given 2D section profile includes camber $\widetilde{f}(x/c)/c$, ideal angle of attack $\widetilde{\alpha}_I$, and ideal lift coefficient $\widetilde{C}_{L_I}$, which all scale linearly with the camber ratio, $\widetilde{f}_0/c$ (Abbott and Doenhoff, 1959). The desired scaling is such that $C_{L_0} = C_{L_I}$ and $\alpha_0 = \alpha_I$,

$$\left\{C_{L_0}, \alpha_0, \frac{f_0}{c}\right\} = \frac{C_{L_0}}{\widetilde{C}_{L_I}} \cdot \left\{\widetilde{C}_{L_I}, \widetilde{\alpha}_I, \frac{\widetilde{f}_0}{c}\right\} \tag{5.1}$$

The pitch angle of the blade section is then fixed at

$$\theta_0 = \beta_{i_0} + \alpha_0 \tag{5.2}$$

These geometry-performance relations can easily be inverted to infer an assumed performance for a given propeller geometry $\{f_0/c,\, \theta_0\}$, in which case

$$\left\{C_{L_0}, \alpha_0, \frac{f_0}{c}\right\} = \frac{f_0/c}{\widetilde{f}_0/c} \cdot \left\{\widetilde{C}_{L_I}, \widetilde{\alpha}_I, \frac{\widetilde{f}_0}{c}\right\} \tag{5.3}$$

It is assumed that $C_L = C_{L_0}$ when $\alpha = \alpha_0$ (i.e. when $\beta_i = \beta_{i_0} = \theta_0 - \alpha_0$).

5.2 Lifting-surface geometry corrections

It is well known that due to flow curvature, thickness/load coupling, and viscous effects, a propeller built according to (5.1) and (5.2) will not have the desired performance, and lifting-surface geometry corrections must be employed if a physical prototype is to be built and tested.

Lifting-surface geometry corrections are required for both the construction of physical prototypes as well as the analysis of an actual 3D propeller geometry. Morgan et al (1968) give corrections to the camber and ideal angle of attack required to construct the 3D blade from 2D lifting-line results. Given the loading at the design point, (5.1) can be used to find $\left\{(C_{L_0})^{2D}, (\alpha_0)^{2D}, (f_0/c)^{2D}\right\}$. Then, the required 3D propeller geometry $\left\{(\theta_0)^{3D}, (f_0/c)^{3D}\right\}$ is:

$$\begin{aligned} (f_0/c)^{3D} &= k_c\ (f_0/c)^{2D} \\ (\alpha_0)^{3D} &= k_a\ (\alpha_0)^{2D} + k_t \cdot \mathrm{BTF} \\ (\theta_0)^{3D} &= \beta_{i_0} + (\alpha_0)^{3D} \end{aligned} \tag{5.4}$$

where k_c is the camber correction due to flow curvature ($0.8 < k_c < 3.5$), k_a is the ideal angle correction due to flow curvature ($1 < k_a < 3.5$), $k_t \cdot \mathrm{BTF}$ is the ideal angle correction due to thickness ($0 < k_t < 1.8$), and BTF is the blade thickness fraction (projected thickness at the propeller axis normalized by diameter). Morgan et al (1968) provide tables of these correction factors versus (r, β_i, $\mathcal{Z}$, and Expanded Area Ratio).

Alternatively, given the full 3D propeller geometry $\left\{(\theta_0)^{3D}, (f_0/c)^{3D}\right\}$, equation (5.4) can be inverted to infer the 2D section performance,

$$\begin{aligned} (f_0/c)^{2D} &= (1/k_c)\ (f_0/c)^{3D} \\ (C_{L_0})^{2D} &= \frac{(f_0/c)^{2D}}{\widetilde{f}_0/c}\widetilde{C}_{L_I} \\ (\alpha_0)^{3D} &= k_a \frac{(f_0/c)^{2D}}{\widetilde{f}_0/c}\widetilde{\alpha}_I + k_t \mathrm{BTF} \end{aligned} \tag{5.5}$$

It is is now assumed that $C_L = (C_{L_0})^{2D}$ and $\alpha = (\alpha_0)^{3D}$ when $\beta_i = \beta_{i_0} = (\theta_0)^{3D} - (\alpha_0)^{3D}$. The nominal case (of no geometry corrections) is recovered by setting $k_c = 1$, $k_a = 1$, $k_t = 0$, in which case (5.1), (5.2), and (5.3) apply in the performance analysis.

5.3 Rotor performance analysis

The off-design performance of a propeller can be estimated using the following method, which is consistent with the design method described in §3 as well as the geometric representations in §5.1 and §5.2. Together, these form a unified design and analysis platform that can be used for preliminary, parametric design studies.

Each rotor operating state is defined by the inflow profile $\{V_a,\ V_t\}$, rotation rate, ω, and unknown parameters $\{V^*,\ \alpha,\ C_L,\ \Gamma,\ u_a^*,\ u_t^*,\ \beta_i,\ \bar{u}_a^*,\ \bar{u}_t^*\}$. Since there are M blade sections, there are $7M + 2M^2$ unknowns and a system of as many non-linear equations that determine the operating state of the rotor. The method presented herein provides this system of equations, as well as a numerical approach for solving them in the lifting line code.

The required equations for V^*, Γ (in terms of C_L), u_a^*, u_t^*, β_i, $\bar{u}_a^*$, and $\bar{u}_t^*$ are given in §2. As shown in Figure 2, the angle of attack is $\alpha = \theta - \beta_i$. In the case of a controllable-pitch rotor with pitch offset θ_p, the total pitch of the blade section is $\theta(r) = \theta_0(r) + \theta_p$, so the angle of attack is $\alpha = \theta_0 + \theta_p - \beta_i$. Whence, $\alpha - \alpha_0 = \theta_p + \beta_{i_0} - \beta_i$. Thus, inflow angle β_{i_0} forms a reference angle, at which it is assumed that the blade section develops lift coefficient $C_L = C_{L_0}$.

In the design-analysis case, β_{i_0} is known from the design loading, and C_{L_0} can be computed using (2.2). In the geometry-analysis case, C_{L_0}, α_0, and thus β_{i_0} can be deduced from equations (5.3) or (5.5).

The lift and drag polars can be computed using the following model, as illustrated in Figure 11. Defining $\Delta\alpha = \alpha - \alpha_0$ [rad], the lift and drag coefficients are

$$\begin{aligned} C_L = C_{L_0} &+ \tfrac{dC_L}{d\alpha}\Delta\alpha \\ &- \tfrac{dC_L}{d\alpha}(\Delta\alpha - \Delta\alpha_{\text{stall}}) \cdot F(\Delta\alpha - \Delta\alpha_{\text{stall}}) \\ &+ \tfrac{dC_L}{d\alpha}(-\Delta\alpha - \Delta\alpha_{\text{stall}}) \cdot F(-\Delta\alpha - \Delta\alpha_{\text{stall}}) \end{aligned} \tag{5.6}$$

$$\begin{aligned} C_D = C_{D_0} &\\ &+ A \cdot (\Delta\alpha - \Delta\alpha_{\text{stall}}) \cdot F(\Delta\alpha - \Delta\alpha_{\text{stall}}) \\ &+ A \cdot (-\Delta\alpha - \Delta\alpha_{\text{stall}}) \cdot F(-\Delta\alpha - \Delta\alpha_{\text{stall}}) \\ &- 2A \cdot (-\Delta\alpha_{\text{stall}}) \cdot F(-\Delta\alpha_{\text{stall}}) \end{aligned} \tag{5.7}$$

where the auxiliary function $F(x) = \frac{1}{\pi}\arctan(Bx) + \frac{1}{2}$ has limits $F(x \to -\infty) \to 0$ and $F(x \to \infty) \to 1$. Here: $\Delta\alpha_{\text{stall}} = 8\frac{\pi}{180}$ [rad] is the assumed stall angle; $B = 20$ is a stall sharpness parameter; $A = \frac{2 - C_{D_0}}{\frac{\pi}{2} - \Delta\alpha_{\text{stall}}}$ is the drag coefficient post-stall slope; and $\frac{dC_L}{d\alpha}$ is the lift curve slope (taken as 2π unless otherwise specified). Thus $C_L \approx C_{L_0} + \frac{dC_L}{d\alpha}(\alpha - \alpha_0)$ before stall and approximately constant post stall. The drag coefficient is approximately constant until stall and then rises to the canonical value of 2 when the inflow is normal to the blade. This type of model is used in the lifting-line aircraft dynamics code `ASWING` (Drela, 1999).

Since (5.6) models $C_L(\alpha - \alpha_0)$ explicitly, the lift curve slope can be set to account for the finite aspect ratio of the rotor blades. In the present model, the lift curve slope is approximated as that of an elliptically-loaded wing

$$\frac{dC_L}{d\alpha} = \frac{2\pi}{1 + 2/\mathcal{AR}} \tag{5.8}$$

where the aspect ratio of the wing (span^2/area) can be formulated as 2(semi-span)^2/semi-area. Thus, for a rotor blade

$$\mathcal{AR} = \frac{2(R - R_{\text{hub}})^2}{\int_{R_{\text{hub}}}^{R} c(r)\, dr} \tag{5.9}$$

Equations (5.6) through (5.9) offer the flexibility to change the stall angle, lift curve slope, and drag coefficient to more accurately model foil sections of moderate thickness. Furthermore, they could be replaced altogether by tabulated experimental data or by lift and drag polars computed by a 2D foil solver code, such as `VLM2D` (Kerwin, 2007) or `XFOIL` (Drela, 1989).

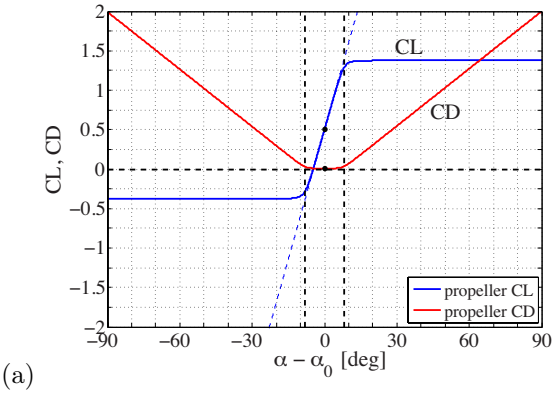

(a)

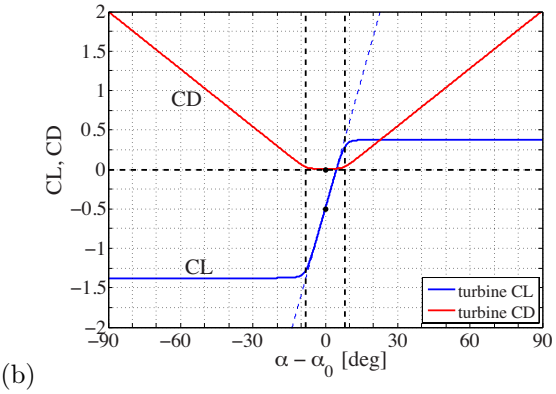

(b)

Figure 11: Lift coefficient, C_L, and drag coefficient, C_D, versus net angle of attack, $\alpha - \alpha_0$, for the (a) propeller and (b) turbine cases, with $\frac{dC_L}{d\alpha} = 2\pi$ and on-design specifications $C_{L_0} = \pm 0.5$ and $C_{D_0} = 0.05$. The vertical dashed lines at $|\alpha - \alpha_I|_{\text{stall}} = \pm 8$ deg indicate the stall angle of attack.

The numerical solution method is as follows. The equations of state can be decoupled by considering two state vectors: $\mathbf{X} = \{V^*, \Delta\alpha, C_L, \Gamma, u_a^*, u_t^*\}$ and $\mathbf{Y} = \{\beta_i, \bar{u}_a^*, \bar{u}_t^*\}$, and the decoupled system can be solved using a Newton solver configured to drive the following

residual vector to zero.

$$\mathbf{R} = \begin{bmatrix} V^* & - & \sqrt{(V_a + u_a^*)^2 + (\omega r + V_t + u_t^*)^2} \\ \Delta\alpha & - & (\theta_p + \beta_{i_0} - \beta_i) \\ C_L & - & C_L(C_{L_0}, \Delta\alpha) \\ \Gamma & - & \left(\frac{1}{2} C_L V^* c\right) \\ u_a^* & - & \left([\bar{u}_a^*] \cdot [\Gamma]\right) \\ u_t^* & - & \left([\bar{u}_t^*] \cdot [\Gamma]\right) \end{bmatrix} \tag{5.10}$$

In order to drive the residuals to zero, the desired change in the state vector, $\mathbf{dX}$, is found by solving

$$0 = \mathbf{R} + \mathbf{J} \cdot \mathbf{dX}$$

where the Jacobian is formed as usual, $\mathbf{J}_{(i,j)} = \frac{\partial \mathbf{R}(i)}{\partial \mathbf{X}(j)}$. The updated state vector is then $\mathbf{X}_{new} = \mathbf{X}_{current} + \mathbf{dX}$.

Between solver iterations, $\{\beta_i,\ \bar{u}_a^*,\ \text{and}\ \bar{u}_t^*\}$ are updated, and iteration continues until convergence of the entire system. For each operating state, the thrust, torque, and efficiency are easily calculated.

This method is essentially that of the blade element momentum (BEM) method, but it offers the advantage that the induced velocities are computed from the vortex lattice and thus, better reflect the load distribution at the lifting line. The key assumption is that the blade develops lift C_{L_0} and drag C_{D_0} when the inflow angle is $\beta_i = \beta_{i_0}$. The lift and drag coefficients for other angles of attack are given by 2D polars, as in BEM.

6 Analysis examples and validation

6.1 Propeller parametric design study

We now continue with the example propeller parametric design study presented in section 4.1. Here, we present the off-design performance analysis, assuming $\frac{dC_L}{d\alpha} = 2\pi$ and ignoring viscous effects ($C_D = 0$). Chord lengths were optimized for each propeller, with $C_{L,\max(r)} = 0.2$. The on-design efficiency of each propeller in this parametric study is shown in Figure 12 '-▼-', which replicates the data in Figure 6.

Figure 12 also shows the off-design performance curves for several of the propellers designed in this study. Using this information, the performance of these propellers can be examined over the entire operational profile of a ship, such as $0.512 \le C_T \le 0.812$ (or the equivalent $K_T = \frac{\pi}{8} C_T \cdot J_s^2$). This operating envelope is shaded in gray in Figure 12.

While prior lifting line codes are typically only used to determine the on-design efficiency, the present unified design-analysis method can be used to seamlessly determine an optimized propeller design and the associated performance curve. This can be quite useful in preliminary design studies, when the designer may know a range of ship C_T values. This off-design performance prediction can tell the designer if the propeller is likely to operate efficiently over its entire operational range.

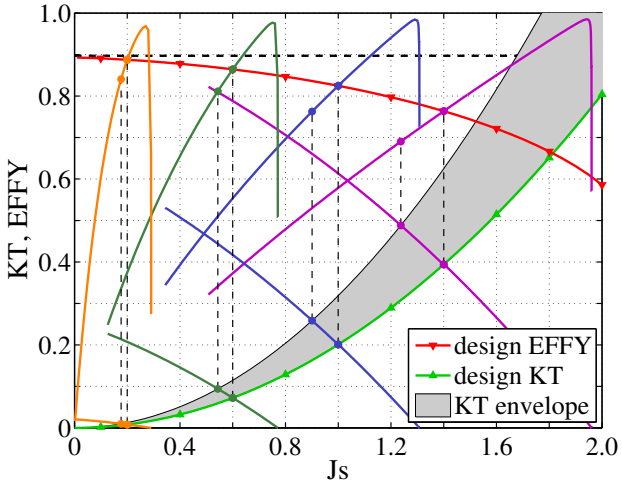

Figure 12: Thrust and eficiency of optimized 5-bladed propellers: '--' actuator disc efficiency; '-▲-' required thrust coefficient $K_T = \frac{\pi}{8} C_T \cdot J_s^2$ on design; '-▼-' efficiency on design; '–' off-design performance curves for propellers with design $J_s = 0.2$, 0.6, 1.0, 1.4, and 1.8.

6.2 DTMB propeller 4119 design replica

David Taylor propeller 4119 (designed by Denny (1968)) is a free-running propeller with a nearly ideal circulation distribution, fair blades, and moderate thickness. Its performance has been well characterized by many workers (Jessup, 1989, e.g.). Here, we design a 4119 replica, given its design specifications: $\mathcal{Z} = 3$, $J_s = 0.833$, $K_T = 0.15$, $V_a/V_s = 1$, and $V_t = 0$. Here, $M = 40$ is used, and the lift curve slope (5.8) was calculated to be $\frac{dC_L}{d\alpha} = 3.1606$. Viscous forces are considered, with $C_D = 0.008$ and the blade outline given in Table 3.

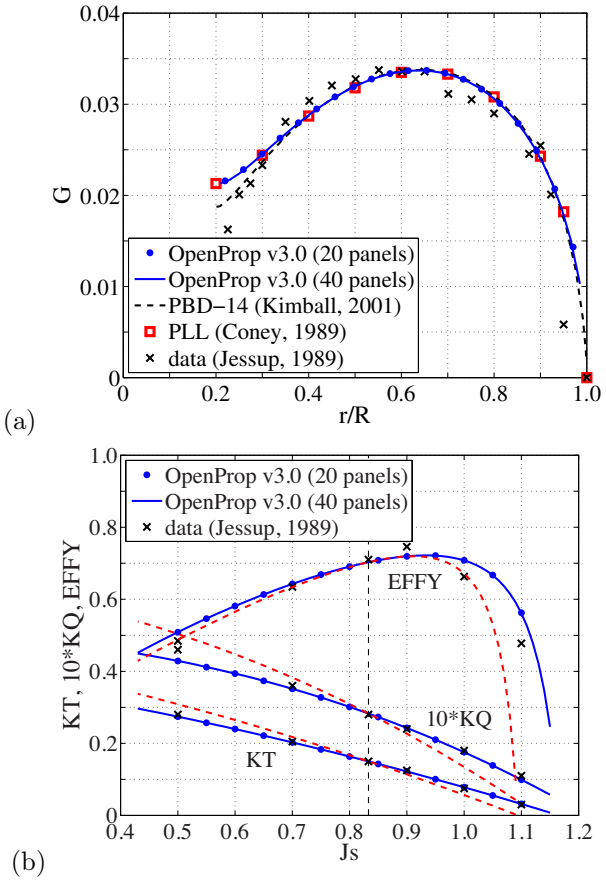

Figure 13: (a) Design circulation distribution for a DTMB propeller 4119 replica, and (b) off-design performance curves. `OpenProp 3.0` ('LL-Linear' method) results agree with `PBD` code (Kimball, 2001) and data from (Jessup, 1989). The red dashed line is the result using $\frac{dC_L}{d\alpha} = 2\pi$, showing the affect of not properly accounting for the lifting surface effects in the performance analysis.

The circulation distribution is plotted in Figure 13a. The `OpenProp 3.0` ('LL-Linear') design agrees well with the lifting line design code `PLL` (Coney, 1989), thus validating the present implementation against the industry standard code. Both lifting-line codes agree well with the lifting surface analysis of `PBD` (Kimball, 2001) and with the experimental data from (Jessup, 1989). This indicates that both the magnitude and distribution of circulation determined by the 'LL-Linear' method are correct. In addition, the `OpenProp 3.0` results with 40 panels agree with those of 20 panels, indicating that the solution is well converged with 20 panels.

Figure 13b shows good agreement between the performance curve predicted by the present method (`OpenProp 3.0`) and the experimental data from (Jessup, 1989). This demonstrates that if the on-design circulation distribution is accurate, then the off-design performance is also accurately predicted by the method in §5.3. Notably, this analysis method does not require knowledge of the actual 3D geometry.

Figure 13b also shows the effect of the choice of lift-curve slope. The performance analysis was repeated with $\frac{dC_L}{d\alpha} = 2\pi$ (i.e. ignoring lifting-surface effects in the off-design performance analysis), and these data are shown as a red dashed line. These results make sense in light of the fact that for J_s less than the advance coefficient at the design point, there are positive net angles of attack, more lift, and thus more thrust and torque. If the lift curve slope is assumed to be 2π as in 2D theory, then the propeller develops more lift (and hence higher K_T and K_Q) than the case where a reasonable $\frac{dC_L}{d\alpha} < 2\pi$ is estimated from (5.8). By setting $\frac{dC_L}{d\alpha}$ using (5.8), the slope of the performance curves $\frac{dK_T}{dJ_s}$ and $\frac{dK_Q}{dJ_s}$ agree well with experimental data, making the performance analysis accurate for a wide range of advance coefficients.

6.3 DTMB propeller 4119 geometry analysis

The performance of propeller 4119 was also estimated from the actual propeller geometry, which is given in Table 3. This propeller employs blade sections with 'NACA a=0.8' meanlines, for which $\widetilde{f_0}/c = 0.0679$, $\widetilde{\alpha}_I = 1.54°$, and $\widetilde{C}_{L_I} = 1$.

r/R	c/D	P/D	f0/c	t0/c
0.2000	0.3200	1.1050	0.0143	0.2055
0.3000	0.3625	1.1020	0.0232	0.1553
0.4000	0.4048	1.0980	0.0230	0.1180
0.5000	0.4392	1.0930	0.0218	0.0902
0.6000	0.4610	1.0880	0.0207	0.0696
0.7000	0.4622	1.0840	0.0200	0.0542
0.8000	0.4347	1.0810	0.0197	0.0421
0.9000	0.3613	1.0790	0.0182	0.0332
0.9500	0.2775	1.0770	0.0163	0.0323
1.0000	0.0020	1.0750	0.0118	0.0316

Table 3: DTRC propeller 4119 geometry

Figure 14a compares the on-design circulation distribution computed using the present geometry analysis method both with and without the (Morgan et al, 1968) lifting surface geometry corrections. While the analysis without the lifting surface corrections grossly over-predicts the loading, use of the (Morgan et al, 1968) corrections result in a circulation distribution that more closely resembles the measured data. For

reference, the '`OpenProp 3.0` replica' from Figure 13 is also included. The data in Figure 14a confirm the well-known fact that lifting surface corrections are required to accurately analyze the performance of a marine propeller using the lifting-line model. Several other lifting surface corrections were coded and tested for both this case and propeller 4381 (see §6.4) (Eckhardt and Morgan, 1955; van Manen, 1957; Cox, 1961; Kerwin and Leopold, 1963). The (Morgan et al, 1968) corrections yielded the most accurate results and thus are used exclusively herein.

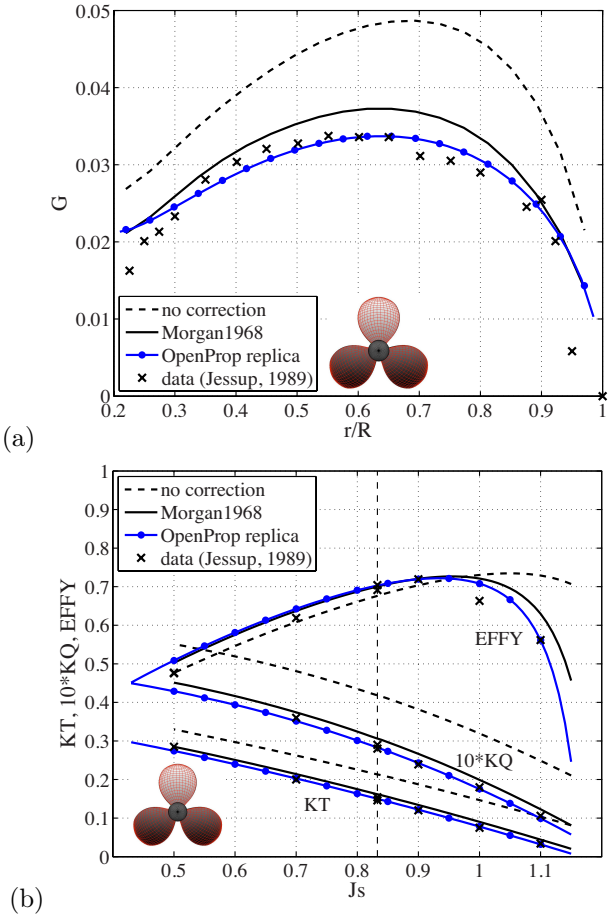

Figure 14: Analysis of the actual DTMB propeller 4119 geometry both without lifting surface geometry corrections '--'; and with the (Morgan et al, 1968) corrections '–': (a) Circulation distribution, and (b) performance curves. For reference, the '`OpenProp 3.0` replica' from Figure 13 is also shown, '-●-'.

Figure 14b shows relatively good agreement between the predicted loads and the measured data when the (Morgan et al, 1968) corrections are used. This figure also illustrates that the thrust and torque coefficient predictions heavily depend on the lifting surface geometry corrections, whereas the efficiency is well estimated regardless of the geometry corrections employed. Thus, the K_T and K_Q differences are due to the camber/pitch corrections, which is a limit of the lifting line method.

Interestingly, the slopes of the performance curves, dK_T/dJ_s and dK_Q/dJ_s, are nearly the same, whether or not the lifting surface corrections are used. This demonstrates that the lifting surface corrections serve to map the given 3D propeller geometry to the performance of the rotor at its design point. The off-design performance predictions parallel one another, regardless of the lifting surface corrections employed.

It is important to reiterate that the '`OpenProp 3.0` replica' is a propeller designed to match the 4119 design point. The present design method (§3.3) resulted in the correct load distribution at the design point, and the analysis method (§5.3) predicted the correct performance for a wide range of advance coefficients. This design and analysis was performed in "design world", with no knowledge of the "real world" geometry required to give such performance. Due to the limitations of the lifting line method, the geometry for the '`OpenProp 3.0` replica' that would be predicted by (§5.2) would be somewhat different than the actual 4119 propeller geometry. Similarly, the performance analysis of the actual 4119 geometry yielded results that were somewhat different than the measured performance. Thus, the limitation of the lifting line method is in mapping from the "design world" performance of a rotor to the "real world" geometry of this rotor, and visa versa.

6.4 DTMB propeller 4381 geometry analysis

Another example performance analysis from given propeller geometry is now illustrated using U.S. Navy propeller 4381, whose geometry is given in Table 4. This propeller was selected based on available experimental data for comparison, as well as concurrent efforts in modeling this propeller during crashback maneuvers. DTMB 4381 is a 5-bladed propeller of moderate expanded area and no rake or skew. Detailed geometric characteristics can be found in (Chesnakas et al, 2004). This propeller employs blade sections with 'NACA a=0.8' meanlines, for which $\widetilde{f}_0/c = 0.0679$, $\widetilde{\alpha}_I = 1.54°$, and $\widetilde{C}_{L_I} = 1$. The lift curve slope (5.8) is $\frac{dC_L}{d\alpha} = 3.6703$.

r/R	c/D	P/D	f0/c	t0/c
0.2000	0.1740	1.2600	0.0312	0.2500
0.3000	0.2280	1.3500	0.0369	0.1560
0.4000	0.2750	1.3600	0.0348	0.1070
0.5000	0.3130	1.3400	0.0307	0.0770
0.6000	0.3380	1.2800	0.0244	0.0570
0.7000	0.3480	1.2100	0.0189	0.0420
0.8000	0.3340	1.1400	0.0147	0.0310
0.9000	0.2810	1.0700	0.0122	0.0240
0.9500	0.2190	1.0300	0.0133	0.0260
0.9800	0.1530	1.0100	0.0164	0.0370
0.9900	0.1150	1.0100	0.0211	0.0500
1.0000	0.0000	1.0000	0.0280	0.0700

Table 4: DTRC propeller 4381 geometry

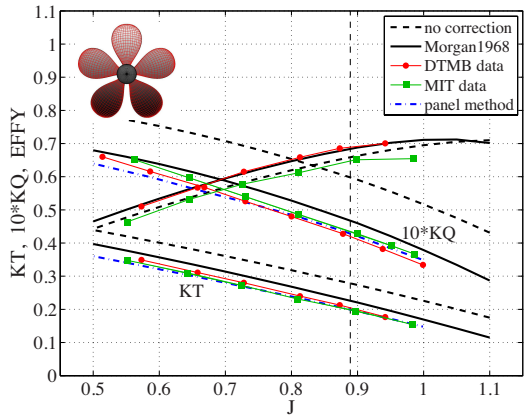

Figure 15: Performance analysis of DTMB propeller 4381, with and without the (Morgan et al, 1968) geometry corrections. Thrust and torque compare well to experimental data from (Greeley and Kerwin, 1982) and panel method analysis from (Brizzolara et al, 2010).

The results in Figure 15 parallel those of Figure 14: namely, the efficiency is fairly accurate when predicted both with or without the lifting surface geometry corrections. While the analysis without the lifting surface corrections grossly over-predicts K_T and K_Q, use of the geometry corrections results in loads that more closely resemble the measured data. This emphasizes that the present lifting line methods can be used to accurately simulate real propeller performance in parametric design studies, but the limitations of the method in simulating an actual geometry is an inherent limit to the lifting line model, and final geometry computations should use a lifting surface method or panel method. Figure 15 shows that the panel method results of (Brizzolara et al, 2010) much more accurately agree with the experimental data, as expected. However, the lifting line design forms a very good starting geometry for a lifting surface design procedure, since the final geometry requires only small changes from the lifting-line geometry to match the required performance.

6.5 Turbine parametric design study

In §4.2, a parametric design study was performed in which several turbines were optimized to maximize power extraction at each of a range of tip-speed ratios. We now continue the example presented in Figure 9, in which we considered both infinite-bladed ($\mathcal{Z} = 100$) and finite-bladed ($\mathcal{Z} = 3$) cases, assuming uniform inflow ($V_a/V_s = 1$, $V_t = 0$), $M = 80$ panels, and a blade root radius of $R_{hub}/R = 0.005$. No hub image was used.

Figure 16 shows power coefficient versus tip-speed ratio for each of the turbines designed in the inviscid case ($C_D = 0$). Momentum theory is shown as the solid line, and the well-known Betz Limit of $C_P = 16/27 \approx 0.5926$ is reached in the limit of infinite tip speed ratio. The off-design performance of the propellers designed for $\lambda = 2$, 5, and 8 is also shown. Although the chord distribution does not affect the on-design performance in the inviscid case, but it does affect the loading changes at off-design tip-speed ratios. The turbines shown in Figure 16 were designed with $|C_L|_{\max} = 1$, which is a typical turbine section lift coefficient. As expected, for any given tip speed ratio (e.g. $\lambda = 3$), the off-design performance curves (solid lines) never exceed the performance of the turbine optimized for that tip speed ratio. Thus, the design optimization and off-design performance analysis methods are self-consistent and form a unified design and analysis approach.

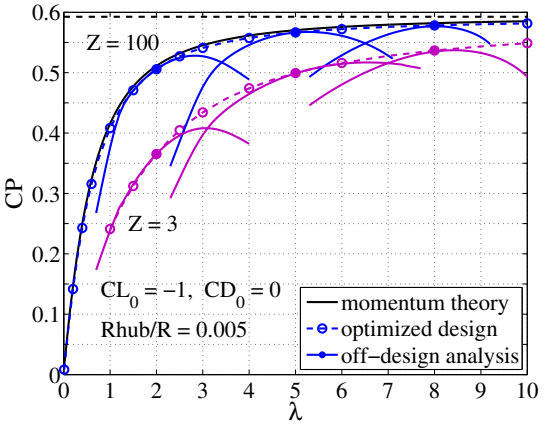

Figure 16: Power coefficient of several turbines at their design point '--o--', as well as the off-design performance of selected turbines '–●–'.

6.6 Turbine design example

Figure 17 shows the performance curves for a viscous case ($C_{D_0} = 0.01$), with three blades and all other parameters the same as above. Three turbines are shown, which were designed with $|C_L|_{\max} = 0.5$, 1, and 2. Figure 17a demonstrates that although a higher design-point lift coefficient yields better on-design performance, the performance gains may be limited to a narrow range of tip-speed ratios. This is due to the shorter chord length blades in the high-C_{L_0} case, which are more greatly affected by changes in angle of attack due to tip-speed ratio changes. In this example, the turbine designed with $C_{L_0} = -1.0$ strikes a balance between performance on- and off-design.

The blade outlines shown in Figure 17b are not reasonable (especially near the root), so a thorough design study would explore other blade shapes, possibly to enhance structural rigidity or reduce weight. For any given blade outline, the parametric design study can be repeated, finding the optimized load distribution for each tip speed ratio, and the off-design performance of each of these turbines.

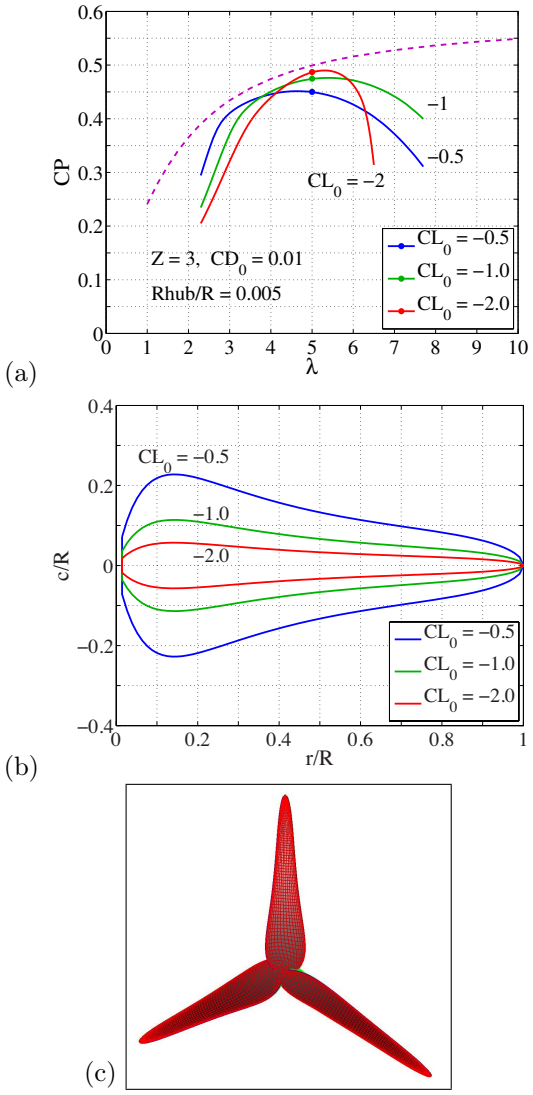

Figure 17: (a) Power coefficient for turbines designed for $\lambda = 5$ with $C_{D_0} = 0.01$ and lift coefficient C_{L_0} as shown. The dashed curve is the on-design limit of $C_{D_0}/C_{L_0} = 0$. The $C_{L_0} = -1$ turbine strikes a balance between performance on- and off-design. (b) Blade outline. (c) 3D rendering of the $C_{L_0} = -1$ turbine.

7 Summary

A unified lifting line method for the design and analysis of axial flow propellers and turbines has been presented. Improvements to the numerical implementation of the lifting line design approach have been described and validated. The extension of the lifting line procedure for analysis for propellers and turbine performance has been described and validated, which greatly extends the usefulness of the method in practice.

This unified method has been shown to be a foundation method for which additional capabilities are easily added. Extensions that have been implemented include: multi-component design, ducted rotor design and analysis, cavitation analysis, blade stress analysis, blade geometry generation, and performance analysis of given geometry. The effect of expanding or contracting wakes can easily be handled in the lifting line model by simply computing the horseshoe influence functions ($\bar{u}_a^*$ and $\bar{u}_t^*$) using a discretized vortex lattice wake. Effects such as unsteady inflow and wake roll-up can also easily be handled in this way.

The method as described can also serve as a computation engine that can be used in system design/analysis suites such as: ship propeller parametric design suites; cavitation and blade strength analysis marine hydrokinetic turbines; and design of controllable-pitch propellers and turbines. In addition the methods describe can serve a basis for more sophisticated tools such as: coupled blade aeroelastic/fluid interaction analysis; unsteady analysis of propellers and turbines including spatially and temporally varying inflow; or floating offshore wind turbine dynamic models.

8 Appendix A: alternative hybrid optimization approach

One might be tempted to use the following assumptions as an alternative hybrid approach, as these may be more in line with the lifting line model

$$\begin{aligned}
\frac{\partial u_a^*(m)}{\partial \Gamma_{(i)}} &= \frac{\partial u_a^*(m)}{\partial u_t^*(m)} \bar{u}_t^*{}_{(m,i)} \\
\frac{\partial u_t^*(m)}{\partial \Gamma_{(i)}} &= \bar{u}_t^*{}_{(m,i)} \\
\frac{\partial V^*(m)}{\partial \Gamma_{(i)}} &= \left(\sin\beta_{i(m)} \, \frac{\partial u_a^*(m)}{\partial u_t^*(m)} + \cos\beta_{i(m)} \right) \bar{u}_t^*{}_{(m,i)}
\end{aligned} \tag{8.1}$$

which results in the following system of optimization equations for the propeller case

$$\begin{aligned}
&(V_{a(i)} + u_a^*{}_{(i)}) r_{c(i)} \triangle r_{v(i)} \\
&+ \sum_m \frac{\partial u_a^*(m)}{\partial u_t^*(m)} \bar{u}_t^*{}_{(m,i)} \, \Gamma_{(m)} r_{c(m)} \triangle r_{v(m)} \\
&+ \sum_m \tfrac{1}{2} C_{D(m)} c_{(m)} \frac{\partial V^*(m)}{\partial \Gamma_{(i)}} [\omega r_{c(m)} + u_t^*{}_{(m)}] r_{c(m)} \triangle r_{v(m)} \\
&+ \sum_m \tfrac{1}{2} C_{D(m)} c_{(m)} V^*{}_{(m)} [\bar{u}_t^*{}_{(m,i)}] r_{c(m)} \triangle r_{v(m)} \\
&+ \lambda_1 [\omega r_{c(i)} + u_t^*{}_{(i)}] \triangle r_{v(i)} \\
&+ \lambda_1 \sum_m \bar{u}_t^*{}_{(m,i)} \, \Gamma_{(m)} \triangle r_{v(m)} \\
&- \lambda_1 \sum_m \tfrac{1}{2} C_{D(m)} c_{(m)} \frac{\partial V^*(m)}{\partial \Gamma_{(i)}} \left[V_{a(m)} + u_a^*{}_{(m)} \right] \triangle r_{v(m)} \\
&- \lambda_1 \sum_m \tfrac{1}{2} C_{D(m)} c_{(m)} V^*{}_{(m)} \left[\frac{\partial u_a^*(m)}{\partial u_t^*(m)} \bar{u}_t^*{}_{(m,i)} \right] \triangle r_{v(m)} \\
&\qquad = 0 \quad \text{for} \quad i = 1 \ldots M
\end{aligned}$$

$$\begin{aligned}
&\sum_m [\omega \, r_{c(m)} + u_t^*{}_{(m)}] \Gamma_{(m)} \triangle r_{v(m)} \\
&- \sum_m \tfrac{1}{2} C_{D(m)} c_{(m)} V^*{}_{(m)} [V_{a(m)} + u_a^*{}_{(m)}] \triangle r_{v(m)} \\
&\qquad = T_s / (\rho \mathcal{Z})
\end{aligned} \tag{8.2}$$

and an analogous system for the turbine case. Indeed, it was found that propeller optimization via (8.2) converged to essentially the same answer as the traditional propeller lifting line approach (3.10) for many cases. However, the analogous turbine code was unstable and often crashed.

9 Appendix B: turbine drag treatment

There exists a fundamental difference in the way that viscous losses are accounted for in lifting line theory versus momentum theory. In lifting line theory, C_D is assumed constant, regardless of C_L, whereas in momentum theory, the ratio $\frac{C_D}{C_L}$ is assumed constant. (Abbott and Doenhoff, 1959, p.148-150) show that for any family of airfoils (e.g. NACA 65-series), the camber ratio (i.e. lift coefficient on design) has little effect on the minimum section drag coefficient. This supports the assumption of constant C_D, which is why that is used in deriving the equations herein. Nevertheless, the optimization equations may be derived assuming $\frac{C_D}{C_L}$ = constant, as will now be shown.

Assuming $\frac{C_D}{C_L}$ = constant amounts to implicitly assuming chord length optimization via equation (3.1). In that case, the "optimum" chord length $c = 2\Gamma/(V^* C_L)$ is chosen to hold C_L and thus $\frac{C_D}{C_L}$ constant. This chord length optimization is made implicit by eliminating c from rotor optimization equations (3.7) and (3.8) via $\frac{1}{2} V^* C_D c = \frac{C_D}{C_L} \Gamma$, which clearly follows from above. With this implicit chord length optimization, the thrust and torque become (again assuming $V_t = 0$ without loss of generality)

$$\frac{T}{\rho \mathcal{Z}} = \sum_{m=1}^{M} \left\{ [\omega r_c + u_t^*] - \tfrac{C_D}{C_L} [V_a + u_a^*] \right\} \Gamma \triangle r_v \tag{9.1}$$

$$\frac{Q}{\rho \mathcal{Z}} = \sum_{m=1}^{M} \left\{ [V_a + u_a^*] + \tfrac{C_D}{C_L} [\omega r_c + u_t^*] \right\} \Gamma \, r_c \triangle r_v \tag{9.2}$$

Now, the turbine design problem is to find the optimum circulation distribution, Γ, such that power extraction is maximized for a given inflow (V_a, ω) and viscous losses ($\frac{C_D}{C_L}$). We again employ the hybrid assumptions (3.22) as well as the turbine constraint (3.20), but now with $\frac{C_D}{C_L}$ = constant, the turbine optimization equations (3.6) become

$$\begin{aligned}
&\left\{ [V_{a(i)} + u_a^*{}_{(i)}] + \tfrac{C_D}{C_L} [\omega r_{c(i)} + u_t^*{}_{(i)}] \right\} \\
&+ \left\{ \tfrac{\partial u_a^*(i)}{\partial u_t^*(i)} u_t^*{}_{(i)} + \tfrac{C_D}{C_L} u_t^*{}_{(i)} \right\} \\
&\qquad = 0 \quad \text{for} \quad i = 1 \ldots M
\end{aligned} \tag{9.3}$$

Comparing (9.3) and the original hybrid optimization equations (3.25), it is evident that these two methods are equivalent when chord optimization via (3.1) is employed.

However, the constant C_D formulation given in §3 affords the flexibility for other chord length optimization methods (Epps et al, 2011, e.g.), or for optimizing blade loading for a fixed blade outline.

References

Abbott, I.H. and von Doenhoff, A.E. (1959) Theory of Wing Sections. Dover.

ABS (2007) Rules for Building and Classing Steel Vessels. American Bureau of Shipping.

Betz A. (1919) "Schraubenpropeller mit geringstem energieverlust", *K. Ges. Wiss. Gottingen Nachr. Math.-Phys. Klasse*, pp 193–217.

Brizzolara S., Villa D., and Gaggero S. (2010) "A systematic comparison between RANS and panel methods for propeller analysis", 9th International Conference on Hydrodynamics (ICHD2010).

Brockett, T.E. (1966) "Minimum Pressure Envelopes for Modified NACA-66 Sections with NACA a=0.8 Camber and Buships Type I and Type II Sections". DTMB Report 1780, Carderock, MD.

Buhl M. (2011) NTWC Design Codes (WT_perf). http://wind.nrel.gov/designcodes/simulators/wtperf/

Burton, Sharpe, Jenkins, and Bossanyi (2001) Wind Energy Handbook. Wiley

Chesnakas, C. and Jessup, S. (1998) "Cavitation and 3-D LDV Tip-Flowfield Measurements of Propeller 5168". Tech. Rep., Naval Surface Warfare Center, Carderock, MD.

Chesnakas C., Donnelly M., Fry D., Jessup S., Park J. (2004) "Performance of Propeller 4381 in Crashback", Tech. Rep. NSWCCD-50-TR-2004/010, Naval Surface Warfare Center, Carderock, MD..

Coney, W.B. (1989) A Method for the Design of a Class of Optimum Marine Propulsors, Ph.D. thesis, MIT, Cambridge, MA.

Cox G. (1961) "Corrections to the camber of constant pitch propellers". Transactions of the Royal Institution of Naval Architects 103(3):227–243.

Denny S.B. (1968) "Cavitation and open-water performance tests of a series of propellers designed by lifting-surface methods", Tech. Rep. Naval Ship Research and Development Center.

Drela M. (1989) "XFOIL: An analysis and design system for low Reynolds number airfoils". In: Low Reynolds Number Aerodynamics: Proceedings for the Conference, Notre Dame, Springer-Verlag.

Drela M. (1999) "Integrated simulation model for preliminary aerodynamic, structural, and control-law design of aircraft". AIAA SDM Conference, 99-1394.

Eckhardt M., Morgan W. (1955) "A propeller design method". SNAME Transactions.

Epps B., Stanway M., and Kimball R. (2009) "OpenProp: An open-source design tool for propellers and turbines". SNAME Propellers and Shafting, Williamsburg, VA.

Epps B.P., Chalfant J.S., Kimball R.W., Techet A.H., Flood, K., and Chryssostomidis C. (2009) "OpenProp: An Open-Source Parametric Design and Analysis Tool for Propellers". Proc. Grand Challenges in Modeling and Simulation, Istanbul, Turkey.

Epps B. (2010a) An Impulse Framework for Hydrodynamic Force Analysis: Fish Propulsion, Water Entry of Spheres, and Marine Propellers. Ph.D. thesis, MIT, Cambridge, MA.

Epps B. (2010b) "OpenProp v2.4 Theory Document". Tech. rep., MIT, http://openprop.mit.edu.

Epps B., Víquez O., and Chryssostomidis C. (2011) "Dual-operating-point blade optimization for high-speed propellers". 11th International Conference on Fast Sea Transportation (FAST 2011), Honolulu, HI.

Epps B. (2013) "An improved wake model that enables propeller lifting line design for bollard pull". Submitted for peer review.

Epps B. and Kimball R. (2013) OpenProp v3: Open-source software for the design and analysis of marine propellers and horizontal-axis turbines. http://engineering.dartmouth.edu/epps/openprop

Falcão de Campos J. (2007) "Hydrodynamic power optimization of a horizontal axis marine current turbine with a lifting line theory". Proceedings of the 17th International Offshore and Polar Engineering Conference, Lisbon, Portugal.

Glauert H. (1935) *Airplane propellers*. In: Durand W. (ed) Aerodynamic Theory: A General Review of Progress, vol 4, Springer.

Greeley D.S. and Kerwin J.E. (1982) "Numerical methods for propeller design and analysis in steady flow". SNAME Transactions vol 90.

Hansen M.O. (2008) Aerodynamics of Wind Turbines. Earthscan.

Hough G.R. and Ordway D.E. (1964) "The Generalized Actuator Disk", Tech. Rep. TAR-TR 6401, Therm Advance Research

Jessup S. (1989) An Experimental Investigation of Viscous Aspects of Propeller Blade Flow. Ph.D. thesis, The Catholic University of America.

Kerwin and Leopold (1963) "Propeller incidence correction due to blade thickness". Journal of Ship Research **2**(7):1–6

Kerwin J.E. (2007) Hydrofoils and Propellers. MIT Course 2.23 notes.

Kerwin J. and Hadler J. (2010) Principles of Naval Architecture: Propulsion. SNAME.

Kerwin J.E., Coney W.B., and Hsin C.Y. (1986) "Optimum circulation distributions for single and multi-component propulsors". Twenty-First American Towing Tank Conference, pp.53–62.

Kerwin K. (1959) "Machine computation of marine propeller characteristics". International Ship Building Progress **6**(60):343–354

Ketcham J. (2010) "Design, build and test of an axial flow hydrokinetic turbine with fatigue analysis". Master's thesis, MIT, Cambridge, MA

Kimball R. (2001) Experimental investigations and numerical modelling of a mixed flow marine waterjet. Ph.D. thesis, MIT

Kinnas S. and Coney W. (1992) "The generalized image model - an application to the design of ducted propellers". Journal of Ship Research **36**:197–209

Kinnas S., Xu W., Yu Y.H., and Lei H. (2012) "Computational methods for the design and prediction of performance of tidal turbines". Journal of Offshore Mechanics and Arctic Engineering (OMAE), vol 134.

Kravitz E. (2011) "Analysis and experiments for contra-rotating propeller". M.s. thesis, MIT.

Laskos D. (2010) "Design and cavitation performance of contra-rotating propellers". Master's thesis, MIT.

Lerbs H. (1952) "Moderately loaded propellers with a finite number of blades and an arbitrary distribution of circulation". SNAME Transactions **60**.

Manwell J., McGowan J., Rogers A. (2009) Wind Energy Explained: Theory, Design and Application. Wiley.

Morgan W., Silovic V., and Denny S. (1968) "Propeller lifting-surface corrections". SNAME Transactions **76**:308–347

Sale D. (2010) NWTC Design Codes (HARP_Opt). http://wind.nrel.gov/designcodes/simulators/HARP_Opt

Stewart H.J. (1976) "Dual optimum aerodynamic design for a conventional windmill". AIAA Journal **14**(11):1524–1527

Stubblefield J.M. (2008) "Numerically based ducted propeller design using vortex lattice lifting line theory". Master's thesis, MIT.

Taylor T. (1996) Preliminary design and analysis of propulsors for axisymmetric underwater vehicles. Ph.D. thesis, MIT

van Manen J.D. (1957) "Fundamentals of ship resistance and propulsion. Part B: Propulsion". In: Publ. No. 132A, Netherlands Ship Model Basin, Wageningen

Wrench J.W. (1957) "The calculation of propeller induction factors". Tech. Rep. 1116, David Taylor Model Basin

Xu W. and Kinnas S. (2010) "Performance prediction and design of marine current turbines in the presence of cavitation". SNAME Transactions **118**.